Materials & Design 209 (2021) 109997

Contents lists available at ScienceDirect

Materials & Design

journal homepage: www.elsevier.com/locate/matdes

Revealing joining mechanism in refill friction stir spot welding of AZ31 magnesium alloy to galvanized DP600 steel

Banglong Fu [a,*], Junjun Shen [a,*], Uceu F.H.R. Suhuddin [a], Ayrton A.C. Pereira [a], Emad Maawad [b], Jorge F. dos Santos [a], Benjamin Klusemann [a,c], Michael Rethmeier [d,e]

[a] Helmholtz-Zentrum Hereon, Institute of Materials Mechanics, Solid State Materials Processing, Max-Planck-Str. 1, Geesthacht 21502, Germany
[b] Helmholtz-Zentrum Hereon, Institute of Materials Physics, X-Ray Diffraction with Synchrotron Radiation, Max-Planck-Str. 1, Geesthacht 21502, Germany
[c] Leuphana University of Lüneburg, Institute of Product and Process Innovation, Universitätsallee 1, Lüneburg 21335, Germany
[d] Technical University Berlin, Institute for Machine Tools and Factory Management (IWF), Pascalstr. 8-9, Berlin 10587, Germany
[e] BAM Bundesanstalt für Materialforschung und -prüfung, Unter den Eichen 87, Berlin 12205, Germany

HIGHLIGHTS

- Refill friction stir spot welding (refill FSSW) was successfully employed to weld AZ31 Mg alloy to galvanized DP600 steel for the first time.
- Defect-free Mg/steel refill FSSW welds with excellent strength were obtained in a wide parameter window.
- The "microstructure-strength-failure" observation revealed the joining mainly attributed to brazing and diffusion welding.
- The growth of Fe-Al intermetallic compounds layer was identified, implying the important role of Al present in Mg alloy for obtaining high-performance welds.

GRAPHICAL ABSTRACT

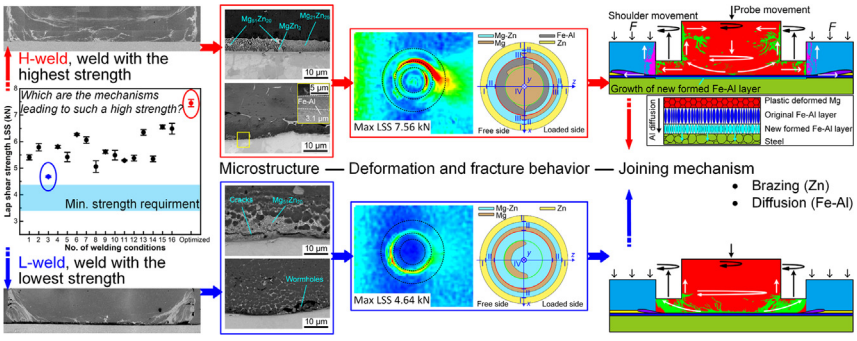

ARTICLE INFO

Article history:
Received 23 February 2021
Revised 5 July 2021
Accepted 19 July 2021
Available online 22 July 2021

Keywords:
Refill friction stir spot welding
Multi-materials joining
Magnesium alloy
Galvanized steel
Microstructure
Mechanical properties

ABSTRACT

The application of magnesium (Mg) inevitably involves dissimilar welding with steel. A novel solid state spot welding method, refill friction stir spot welding (refill FSSW), was utilized to weld AZ31 Mg alloy to galvanized DP600 steel. Although Mg/Fe is an immiscible alloy system, defect-free welds with high strength were successfully obtained in a wide parameter window. The results of microstructure, interfacial reactions, and mechanical properties are reported to reveal the underlying joining mechanism. Due to the melting of Zn coating and subsequent Mg-Zn reactions, Mg-Zn eutectic and intermetallic compounds were detected within welds. Heterogeneous interfacial reactions occur along Mg/steel interface, and the relationship between interfacial structure and fracture behavior was investigated. The joining mechanism is associated with Zn coating and Fe-Al layer: 1) the presence of Zn coating is beneficial for achieving high-quality welding between Mg and steel, it protects the interface from oxidation and contributes to brazing of the weld; 2) the Al present in Mg alloy reacts with Fe, resulting in the growth of Fe-Al layer, which contributes to the diffusion bonding in the interface. The overall results clearly show that refill FSSW is a competitive welding method for joining Mg and galvanized steel.

* Corresponding authors.
E-mail addresses: banglong.fu@hereon.de (B. Fu), junjun.shen@hereon.de (J. Shen).

https://doi.org/10.1016/j.matdes.2021.109997
0264-1275/

1. Introduction

Due to the superior properties such as low density, high specific strength and sound damping capability [1,2], magnesium (Mg) alloys have been considered as competitive materials for the automotive industry. Meanwhile, steel remains the dominant and irreplaceable structural material due to its high strength, excellent ductility, and low fabrication cost [3,4]. The hybrid structure of Mg/steel can fulfill the requirements of vehicle weight reduction while maintaining the required load-capacity [5–7]. Consequently, reliable welding technologies for joining Mg to steel need to be developed.

However, the weldability between Mg and steel by conventional fusion welding methods is rather poor considering the large differences in physical and metallurgical properties. Judging from Mg-Fe binary phase diagram [8], the melting point of Fe (1823 K) is even much higher than the boiling point of Mg (1380 K), thus simultaneous melting of both metals is impossible. Furthermore, unlike other dissimilar metals combinations such as Al/Mg, Al/Ti, Al/Fe (steel), which can form solid solutions or intermetallic compounds (IMCs) to achieve metallurgical bonding, Mg/Fe is an immiscible alloy system. Therefore, almost no inter-solubility and reaction between them are present, resulting in significantly increased difficulties for joining Mg to steel. Employing appropriate intermediate elements or interlayers are promising ways to overcome these problems [9–11], and the feasibilities of using Al [12], Zn [13,14], Cu [15,16], Ni [3,17,18] and Sn [4,19] have been investigated. In this regard, Mg/steel continuous welds in butt and lap joint configurations are finally obtained by developed laser-based welding technologies (i.e., laser brazing [4,12,13,17,18], laser-arc hybrid welding [3,16,19]), and by solid state welding processes, such as friction stir welding [5,7,20–22] and friction-stir assisted scribe technique [23,24].

In fact, in most parts of automotive structures, continuous welds are not required, and about 90% of the assembly work is performed by spot welding [25]. However, studies on spot welding of Mg/steel joints are limited. Results of resistance spot welding showed the occurrences of shrinkage cracks and cavities [26] due to melting of Mg. Moreover, the parameter window to obtain defect-free welds are rather narrow [27]. By using solid state spot welding methods such as ultrasonic spot welding [28] or friction stir spot welding (FSSW) [29,30], sound Mg/steel dissimilar welds can be obtained. The investigations of the interfacial microstructure of these studies showed the formation of IMCs such as Mg_7Zn_3, Mg_2Zn_{11}, Mg_2Sn, which are resulted from the metallurgical reactions between Mg and Zn or Sn coating on the steel surface.

Recently, a new solid state spot welding method, refill friction stir spot welding (refill FSSW), developed by Helmholtz-Zentrum Hereon, has attracted much attention from research and industry. The detailed descriptions of the refill FSSW process can be found in previous publications [31–33]. Due to the significant merit of keyhole-free welds compared to the basic FSSW process, Al/Al [31,34,35] and Mg/Mg [36] similar welds with high performance have been successfully obtained by refill FSSW. It also shows remarkable advantages for the welding of dissimilar materials combinations such as Al/Mg [37,38], Al/Cu [39], Al/steel [40–42], Al/Ti [43] and even metal to composite materials [44]. However, considering refill FSSW of Mg/steel joints, only very limited publications can be found in the literature so far. Some preliminary results of refill FSSW of ZEK100 Mg alloy to galvanized steel have been reported [45,46], where voids and cracks were detected in the welds.

In the present study, the feasibility of refill FSSW of the more commonly used Mg alloy AZ31B to galvanized DP600 steel is proven by producing defect-free welds with high lap shear strength (LSS) in a wide parameter window. The joining mechanism is revealed through detailed metallurgical, microstructural and fracture analyses. The encouraging results provide a scientifically sound basis for achieving reliable Mg/steel spot joints, promoting the usage of Mg/steel hybrid structures in industry.

2. Experimental procedures

2 mm thick sheets of commercial AZ31B Mg alloy, measuring 100 mm (length) × 25.4 mm (width) and 1.5 mm thick hot-dip galvanized DP600 steel samples with the same dimensions were used in this study. Their chemical compositions and mechanical properties are listed in Table 1. The corresponding microstructures of the base materials (BMs) are shown in Fig. 1.

The microstructure of AZ31B Mg alloy consists of equiaxed grains with an average grain size of 20 μm, as shown in Fig. 1**(a)**, and fully divorced α-Mg + γ-$Mg_{17}Al_{12}$ eutectics distributed at grain boundaries. The galvanized DP600 steel possesses a uniform and continuous Zn coating with the thickness of 9.7 ± 3.9 μm. An ultra-thin Fe-Al IMCs layer exists between Zn coating and the steel matrix, shown in Fig. 1**(b)**. This reaction layer was formed during the hot-dip galvanizing process and is mainly composed of Fe_2Al_5 [47].

Before welding, the surfaces of both Mg and steel sheets were degreased using acetone. The sheets were then positioned in lap joint configuration with an overlap distance of 25.4 mm, as shown in Fig. 2**(a)**. The tool system, composed of a clamping ring (diameter of 14.5 mm), a shoulder (9 mm) and a probe (6 mm), was assembled to the Harms & Wende RPS 100 welding machine to perform refill FSSW. The shoulder plunge variant [48] was used throughout this study. For the welding parameters, the constant welding force of 10.5 kN was applied, while the effects of rotation speed (RS), plunge depth (PD), plunge time (PT), dwell time (DT) and retraction time (RT) were investigated and optimized by Taguchi method. Each parameter consisted two levels, as summarized in Table 2, and the L_{16} orthogonal array was selected for designing the experiment. The complete experimental table is given in Supplementary **Table S1**.

During welding, the temperature measurements by thermocouples were performed at a sampling frequency of 100 Hz. K-type thermocouples with 0.5 mm diameter were embedded in the steel sheets at a depth of 0.1 mm away from the Mg/steel interface, Fig. 2**(b)**. For comparison, thermal cycles of Mg/Mg and Mg/bare DP600 steel via refill FSSW were also recorded, using the same optimized parameter set of Mg/galvanized steel.

After welding, the samples were sectioned through the weld center, and the cross-sectional specimens (*x*-*y* plane) were prepared according to standard metallographic procedures. The macro/microstructure was analyzed by FEI Quanta 650 field-emission scanning electron microscope (FE-SEM) equipped with EDAX Apollo X energy dispersive X-ray spectroscopy (EDS) capability and Velocity electron backscatter diffraction (EBSD) system. The data of EDS and EBSD was analyzed by EDAX TEAM 4.6 and TSL OIM 7.3, respectively. Moreover, the phases within the weld were identified by high-energy synchrotron X-ray diffraction (HEXRD) technique, which was conducted at P07 beamline of PETRA III, Deutsches Elektronen-Synchrotron (DESY). The experimental system was introduced in the previous publication [70] and the parameters used are listed in Table 3, which give access to the full Debye-Scherrer rings collected in transmission mode with the maximum diffraction angle 2θ of 12°. The raw data was an image containing the 2D diffraction patterns, and was further azimuthally integrated from 0 to 360° using Fit2D [49] to obtain the conventional 1D diffractogram, i.e. intensity against 2θ spectrum. Finally,

Table 1
Chemical compositions and mechanical properties of BMs.

Materials	Chemical composition measured by XRF (wt. %)									Mechanical properties		
	Mg	Fe	Zn	Al	Mn	Si	Cu	P	S	UTS (MPa)	EL (%)	MH ($HV_{0.1}$)
AZ31B	Bal.	–	1.1	3.3	0.3	0.02	0.04	–	–	225	12	57 aver.
DP600	–	Bal.	–	0.03	1.3	0.44	0.02	0.01	0.01	594	22	201 aver.
Zn coating	–	2.24	Bal.	–	–	–	–	–	–	–	–	–

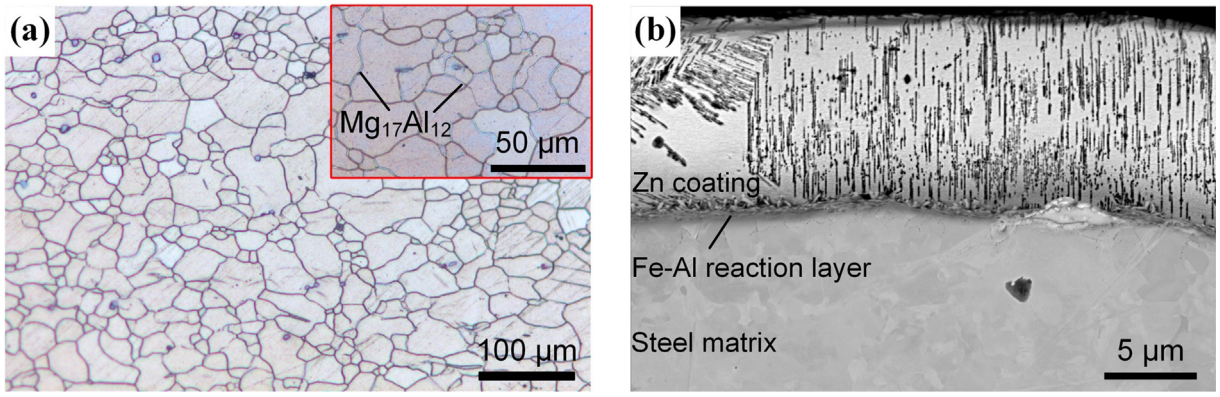

Fig. 1. Microstructure of BMs (a) AZ31B Mg alloy and (b) galvanized DP600 steel.

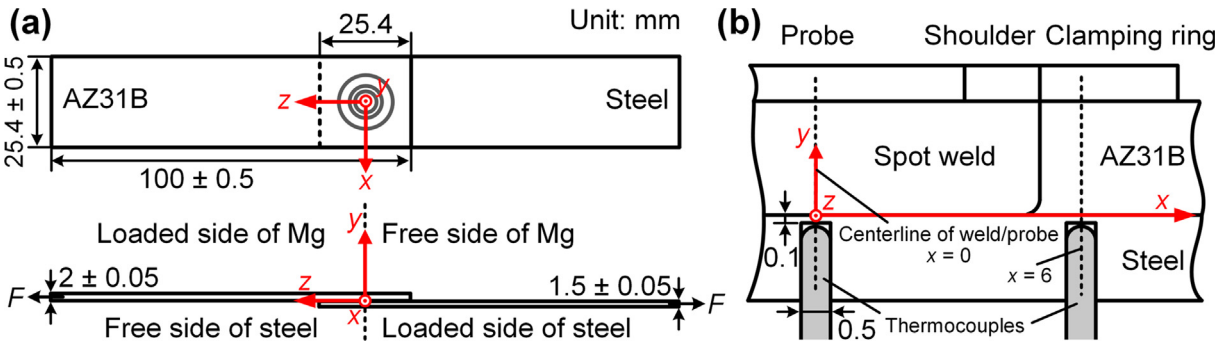

Fig. 2. (a) Refill FSSW lap joint configuration of Mg/steel. (b) Illustration of temperature measurement positions.

Table 2
Welding parameters and the levels investigated with Taguchi method.

Parameter level	Rotation speed	Plunge depth	Plunge time	Dwell time	Retraction time
	RS (rpm)	PD (mm)	PT (s)	DT (s)	RT (s)
−1, low level	1200	1.6	2	0	1
+1, high level	2000	1.9	3	2	2

Table 3
Experimental parameters used for HEXRD analysis.

Calibration	Energy	Wavelength	Beam size	Exposure time	Sample-detector distance	2D Detector
LaB_6	87.1 keV	0.14234 Å	0.5 × 0.5 mm^2	10 s	1314 mm	PerkinElmer XRD 1622

the diffraction peaks were indexed by the program MAUD [50] according to Powder Diffraction Files (PDFs) of interested phases from International Center for Diffraction Data (ICDD) database. Since the referred PDFs are obtained by Cu-Kα1 radiation, the 2θ angles for analysis are calculated as:

$$\theta_{HEXRD} = \sin^{-1}\left(\frac{\sin\theta_{Cu-K\alpha1} \times \lambda_{HEXRD}}{\lambda_{Cu-K\alpha1}}\right) \quad (1)$$

where $2\theta_{HEXRD}$ and $2\theta_{Cu\text{-}K\alpha1}$ are the diffraction angles using HEXRD and Cu-Kα1 X-ray, respectively. The wavelength of HEXRD λ_{HEXRD}, listed in Table 3, is 0.14234 Å, and that of Cu-Kα1 X-ray $\lambda_{Cu\text{-}K\alpha1}$ is 1.54056 Å.

The LSS tests were conducted at room temperature using Zwick/Roell 1478 universal testing machine with a crosshead speed of 1 mm/min. Three repetitions for each parameter combination were conducted. Digital image correlation (DIC) was used to analyze the

spatial deformation behavior of the Mg sheet upper surface during LSS test, and the images were captured at a frame rate of 3 Hz by GOM ARAMIS optical measurement system. Vickers microhardness maps of the cross-sectional surface were obtained using BAQ UT100 microhardness tester under 0.98 N load dwelled for 10 s.

3. Results

The typical Mg/steel weld appearance after refill FSSW is shown in Fig. 3**(a)**. Although traces from the welding tool are present, the weld is characterized by a smooth surface without keyhole, where the overall height variation is within ± 100 μm. The shoulder refill zone is higher than the sheet surface while the probe refill zone is lower, which is related to the shoulder plunge mode used in this study.

The obtained LSS of the welds, performed according to Taguchi method, is given in Fig. 3**(b)**. The strength of all the welds fulfills the requirement of the AWS standard for resistance welding for aerospace applications [51]. Thus, refill FSSW is a feasible and competitive welding method for Mg/steel joints.

Under all the parameter combinations, the final optimized parameter setting is identified as RS = 2000 rpm, PD = 1.9 mm, PT = 3 s, DT = 2 s, RT = 2 s, resulting in the welds with an average maximum LSS of 7.5 kN, Fig. 3**(b)**. These welds are referred as "H-weld" in the following context. Weld produced under the condition RS = 1200 rpm, PD = 1.6 mm, PT = 2 s, DT = 0, RT = 1 s, which resulted in the lowest average LSS, are henceforth referred as "L-weld". In the following, a comparative study is conducted between H-weld and L-weld in terms of macro/microstructure characterization and mechanical properties analysis, to understand the mechanisms leading to the differences observed in the LSS results.

3.1. Macro/microstructure of the welds

The cross-sectional macrostructures of H-weld and L-weld captured by backscatter electrons (BSEs) are shown in Fig. 4**(a) and (b)**. Although a small liquation crack is occasionally observed in the center of the H-welds, most H-welds obtained are defect-free, while in L-welds, severe cavity or void flaws commonly exist.

According to the variation of grain morphology, the weld region in the Mg sheet can be classified into three zones, the heat-affected zone (HAZ), thermo-mechanically affected zone (TMAZ) and stirred zone (SZ). The HAZ of both H-weld and L-weld shows coarser grain size compared to the Mg BM. In contrast, the SZ experiences dynamic recrystallization (DRX), resulting in a substantially refined grain structure with DRX fractions f_{DRX} above 70%, as shown in Fig. 5**(a) and (b)**. Additionally, due to the higher heat input, the H-weld features a larger average grain size of 9.4 μm in the SZ compared to 5.3 μm in the L-weld.

Unlike similar welds, which are characterized by homogenous contrast in the SZ when observed by BSE signal, the SZ of Mg/steel welds presents contrast variations, implying the existence of different phases, as shown in Fig. 4**(a) and (b)**. Thus, chemical composition analysis was performed via EDS to identify the possible phases *qualitatively*. A detailed observation of the zone 1 marked in Fig. 4**(a)**, shown in Fig. 6**(a)**, indicates bright region of significantly higher Zn content (above 4%, reported in atomic percentage at.%, and similarly hereinafter) and the dark region corresponds to the composition of the Mg BM. A much darker region, Fig. 6**(b)**, is observed adjacent to the welding interface, and it consists of high oxygen (O) content mainly resultant from the galvanic corrosion between Mg and steel during the polishing procedure instead of oxidation during welding [52]. Thus, oxygen is neglected to eliminate the disturbance of galvanic corrosion on the composition analysis.

A more detailed observation of the bright region of increased Zn content, shown in Fig. 6**(c)**, reveals that this region can be subdivided into four microregions. The possible phases according to EDS analysis are indicated in each region, the analysis positions and results are summarized in Supplementary **Fig. S1** and **Table S2**, respectively. The region C1 corresponds to the matrix material, which is the primary α-Mg phase. The region C2 is characterized by a lamellar coupled eutectic structure, consisting of eutectic α-Mg (darker region) and $Mg_{51}Zn_{20}$ IMCs (lighter region). A divorced eutectic structure is visible in region C3, where the white isolated island-like phase $Mg_{51}Zn_{20}$ is distributed along the grain boundary of primary α-Mg. For the region C4, although it shows a similar structure to C2, the light phase has been inferred to be $Mg_{21}Zn_{25}$. Judging from the Mg-Zn binary phase diagram [53,54], $Mg_{51}Zn_{20}$ and primary $Mg_{21}Zn_{25}$ are generated by the eutectic reaction: $L \rightarrow Mg_{51}Zn_{20} + Mg_{21}Zn_{25}$ at 615 K, while secondary $Mg_{21}Zn_{25}$ forms due to the following eutectoid reaction: $Mg_{51}Zn_{20} \rightarrow \alpha\text{-Mg} + Mg_{21}Zn_{25}$ at 594 K. The eutectoid transformation is characterized by solid phase decomposition, which usually

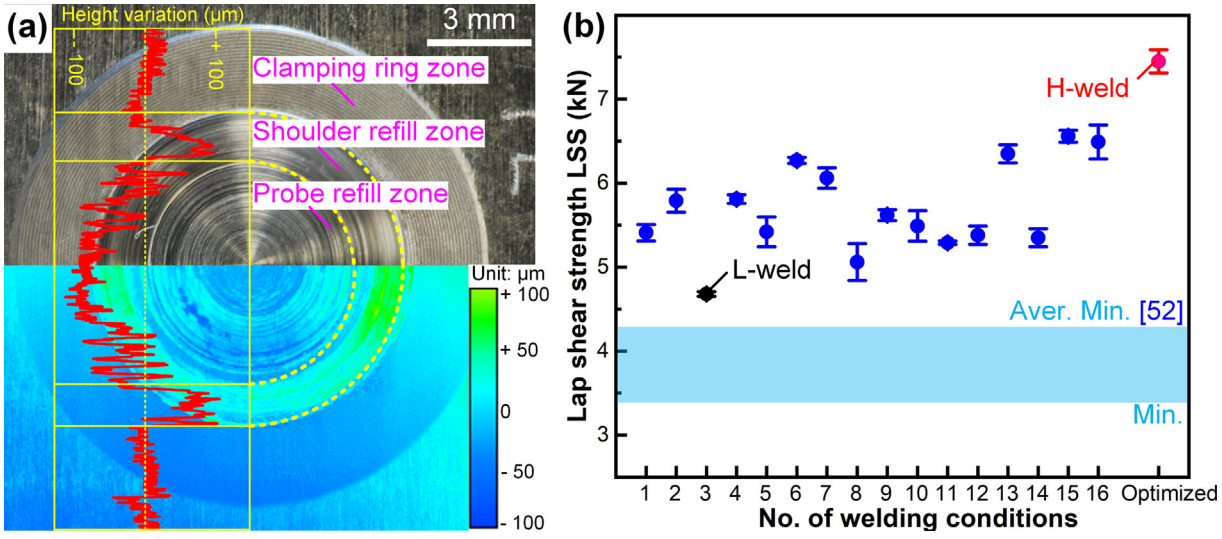

Fig. 3. (a) Surface appearance of a Mg/steel weld, including the surface height variation compared to original sheet surface. (b) LSS for different welding conditions according to Taguchi method and the final optimized weld.

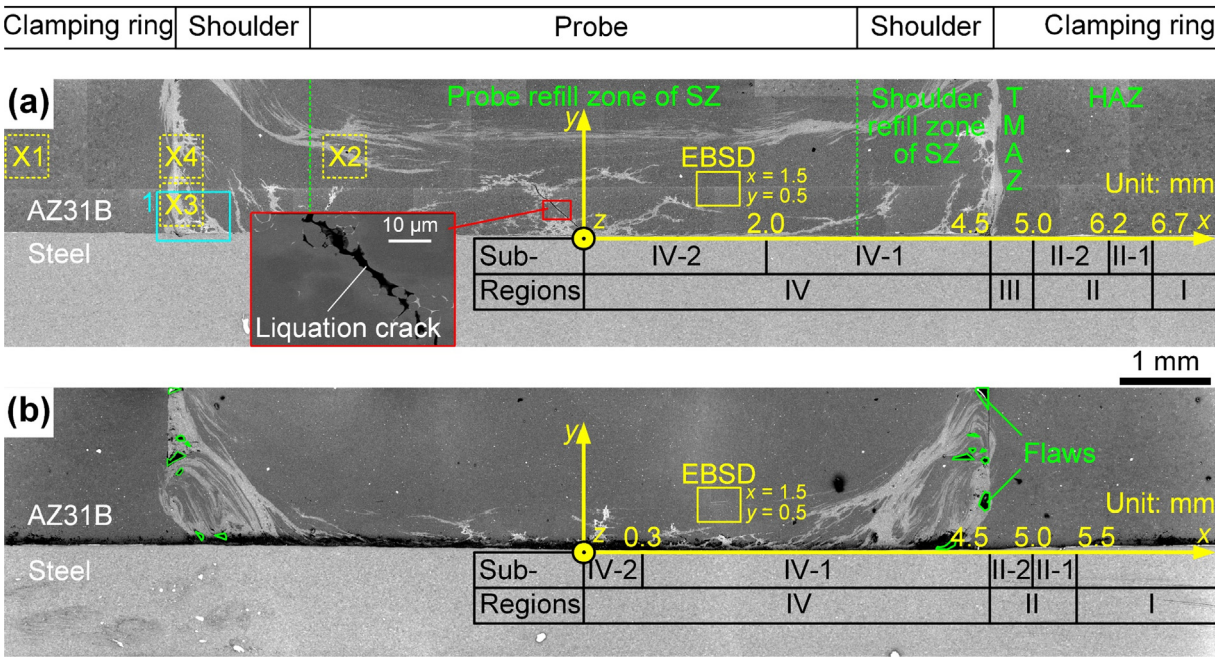

Fig. 4. The cross-sectional macrostructure of (a) H-weld, (b) L-weld. Regions analyzed by EBSD are marked by yellow solid squares, while those analyzed by HEXRD, i.e. X1-X4, are marked by yellow dotted squares. (For interpretation of the references to colour in this figure legend, the reader is referred to the web version of this article.)

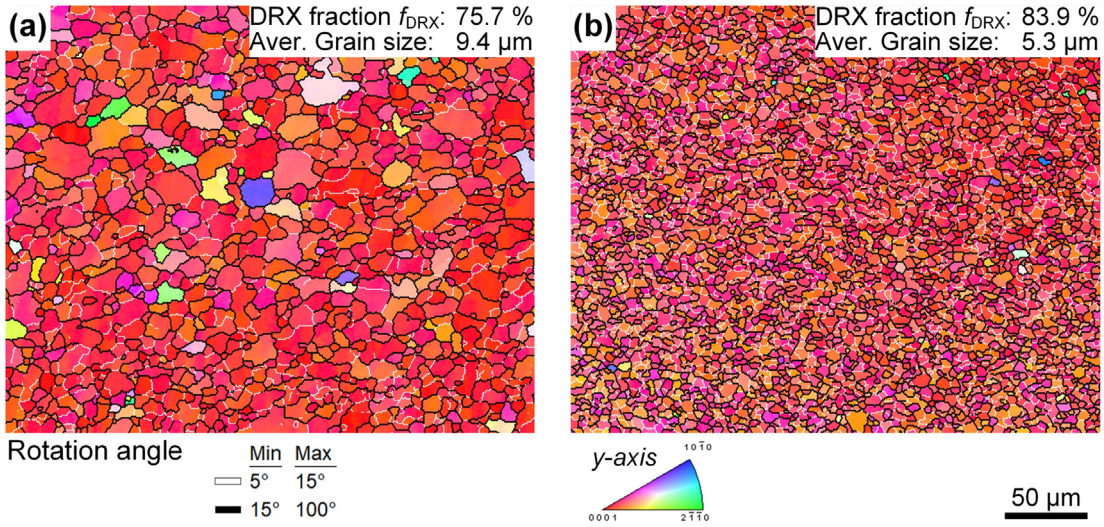

Fig. 5. EBSD map of the SZ of (a) H-weld and (b) L-weld.

results in decreased lamellar spacing compared to the eutectic reaction [55]. A comparison of the lamellar spacing between C2 and C4 implies that C4 mainly represents a eutectoid structure. In addition, in some regions, fine Mg-Zn IMC particles distribute along α-Mg, Fig. 6**(d)**, which is related to the divorced eutectic reaction.

The existence of possible Mg-Zn IMCs as $Mg_{51}Zn_{20}$, $Mg_{21}Zn_{25}$ revealed by EDS is interesting and deserves further identification *reliably* according to crystal data. Thus, the represented zones X1-X4 marked in Fig. 4**(a)** were analyzed by HEXRD, and the resulting patterns are summarized in Fig. 7.

The zone X1, belonging to the Mg BM, shows predominant Mg reflections. However, in zone X2, which is located within the SZ and is characterized with coexistence of bright and light regions, the pattern shows minor diffraction peaks from Zn in addition to the main Mg peaks. The difference between the patterns of X1 and X2 corresponds to the results obtained by SEM-EDS, suggesting that Zn exists in the bright region. The eutectic and eutectoid structures, as shown in Fig. 6**(c)**, are observed within the X3 and X4 zones. The diffraction pattern analysis proves that both zones contain $Mg_{51}Zn_{20}$ and Zn phases, as well as some traces of Mg_4Zn_7, which has not been observed by EDS. In addition, the presence of $Mg_{21}Zn_{25}$ phase is proven in zone X3. Finally, based on the results of EDS and HEXRD, the Mg-Zn IMCs as $Mg_{51}Zn_{20}$, $Mg_{21}Zn_{25}$ and Mg_4Zn_7 are identified.

The formation of different phases in the SZ suggests that during the welding process, the Zn coating on the steel surface reacts with Mg and is transported under the combined effects of heat and intense plastic deformation. Thus, the Zn can be utilized as "tracing element" to reveal the material flow behavior. For the

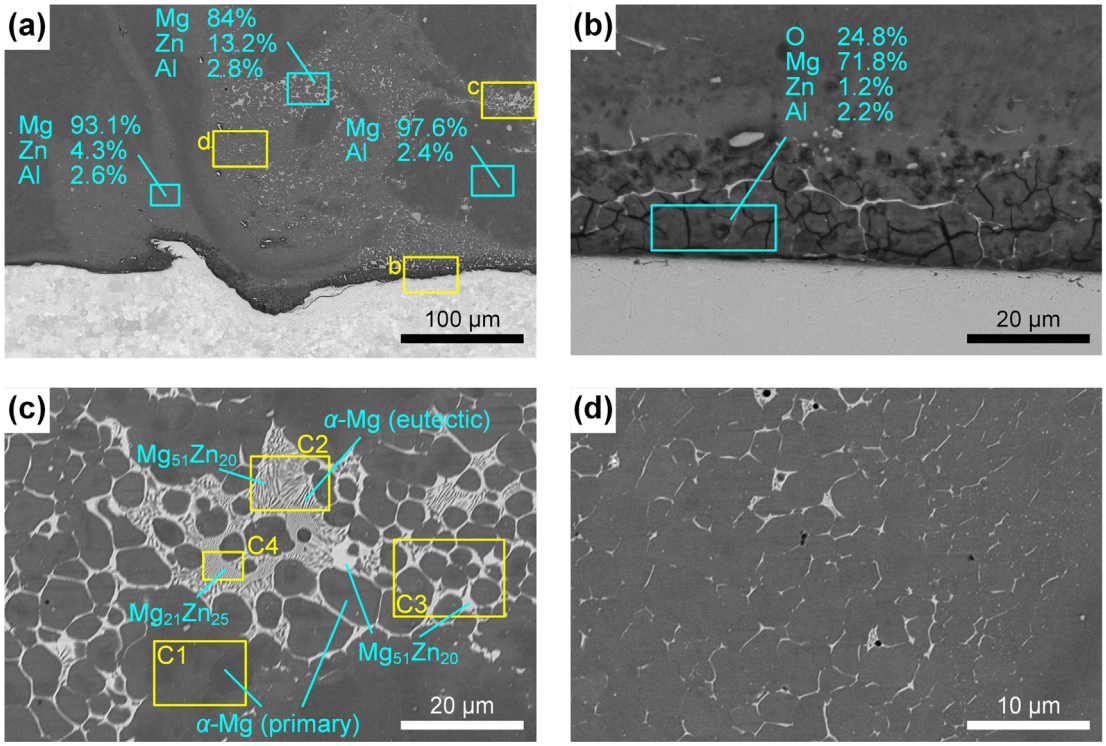

Fig. 6. (a) Higher magnification of zone 1 marked in Fig. 4(a); (b-d), detailed observation of zone b-d marked in (a).

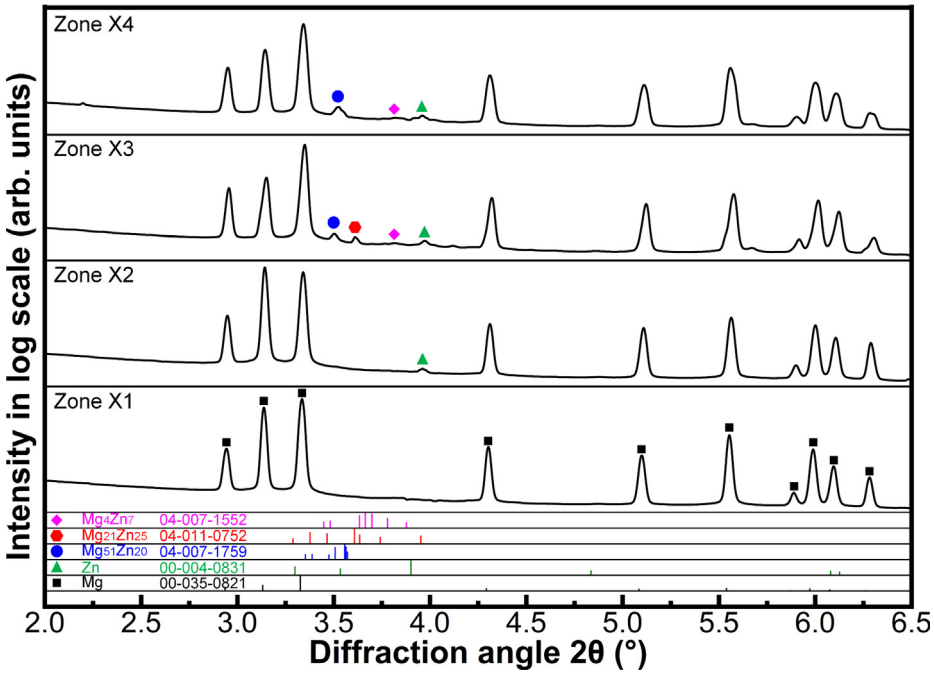

Fig. 7. Indexed HEXRD diffractograms of zones X1-X4, according to Fig. 4(a). The corresponding positions of Bragg peaks, which are calculated according to referred PDFs numbers of ICDD, are also indicated.

H-weld, Fig. 4(**a**), judging from contrast variation, Zn is pushed to the edge of the SZ by shoulder and is also moved into the SZ via the movement of the probe, while for the L-weld, Fig. 4(**b**), Zn is observed mainly in the shoulder refill zone and piles up along the whole welding interface. The effect of material flow on the weld properties and joining mechanisms is discussed in Section 4.2.

3.2. Interfacial structure

For dissimilar welds, the interfacial structure plays a very important role considering that failure usually occurs along the welding interface. Observation on the H-weld suggests that heterogeneous interfacial reactions occur, and the interface can be divided into four regions, i.e. interface I to IV, Fig. 4(**a**). For com-

pleteness, the microstructural features are summarized in Supplementary **Table S3**.

Detailed microstructures of different interfacial regions of H-weld are shown in Fig. 8. The corresponding EDS analysis positions and results are shown in Supplementary **Fig. S2** and **Table S4**, respectively.

(1) The interface I region, Fig. 8**(a)**, represents a region outside the weld within the HAZ of both materials underneath the clamping ring. The original Zn coating cracks under the effect of the clamping ring force and further interlocks with the Mg alloy, providing a weak mechanical interlock.

(2) The interface II region, located closer to the SZ compared to interface I, can be further divided into two sub-regions. For the sub-region II-1, Fig. 8**(b)**, there are two continuous layers at the interface between Mg and steel. The present top grey layer of approximately 2.5 μm thickness is identified as Mg_4Zn_7, while the underlying bright layer is the preserved Zn coating with a little increased Mg content, implying that Mg diffuses into Zn during refill FSSW. In the sub-region II-2, Fig. 8**(c)**, the Zn coating is completely replaced by a Mg-Zn eutectic/eutectoid structure, and Mg-Zn IMCs such as $Mg_{21}Zn_{25}$, $Mg_{51}Zn_{20}$ and $MgZn_2$ are detected.

(3) The region directly adjacent to the SZ is denoted as the interface III region, Fig. 8**(d)**. Since the liquid Mg-Zn eutectics formed during welding are squeezed into interface II, Fig. 8**(c)**, no apparent Zn and Mg-Zn IMCs are found in the interface III region. Instead, Mg is pushed into the slightly deformed steel surface.

(4) The interface IV region represents the interfacial region directly located underneath the SZ, which can be further divided into two sub-regions. Although the set PD of the shoulder is 0.1 mm above the interface, due to the deformation of the sheet surface introduced by material flow and tolerance deviation of the machine during the plunge stage, the bottom of the tool may have touched the steel surface. This results in significant deformation of the steel surface in the sub-region IV-1, Fig. 8**(e)**. Thus, Mg and steel form a micro-interlocked structure, which is beneficial for the bonding strength. In addition, in this region, the Mg-Zn eutectics are transported about 8 μm above the Mg-steel interface by the materials flow. The sub-region IV-2 is near to the weld center, Fig. 8**(f)**. Here the Mg-Zn eutectics decrease significantly, suggesting that the eutectic is transported into the SZ and to the interface II region, which locates outside the spot weld.

Apart from the differences in Zn coating, Mg-Zn eutectics or Mg-Zn IMCs in the interface zones, a detailed investigation of the Mg/steel interface reveals another ultrathin layer with homogenous morphology, as shown in the embedded images in Fig. 8**(b), (d)-(f)**. In the interfacial region II-1, the chemical composition line scan across the interface (L1) illustrates that both Fe and Al contents show a peak in this layer, Fig. 9**(a)**, representing the pre-existing Fe-Al IMC layer on the galvanized steel. The thickness of the Fe-Al layer is found to be always below 1 μm in the interface I to III regions but increases up to 1.9 μm, Fig. 8**(e)**, and even to 3.1 μm, Fig. 8**(f) and 9(b)**, in the interface IV region. The growth of the Fe-Al layer is also verified by the comparison of elemental mappings of interface II and IV regions, shown in Supplementary **Fig. S3**. Thus, diffusion behavior between Al and Fe is identified, which is beneficial for the metallurgical bonding between Mg and steel.

Furthermore, the complementary HEXRD observation was performed in different interfacial regions to obtain a deeper understanding of the interfacial reaction and identify the possible phases proposed by EDS. The resulting diffraction patterns along the interface are shown in Fig. 10. All the patterns obtained reveal dominant peaks corresponding to Mg, α- and γ-Fe phases, where the minor diffraction peaks vary with the measured positions. In interface I region, the minor peaks (2θ of 3.53° and 4.8°) are identified as Zn, which is in good agreement with the microscopy analysis, shown in Fig. 8**(a)**. From interface II-1 to interface II-2, as approaching the SZ, the gradual disappearance of Zn due to Mg-Zn reactions, as shown in Fig. 8**(b) and (c)**, is also indicated by HEXRD, where the peaks corresponding to the Mg-Zn IMCs, i.e. $Mg_{51}Zn_{20}$ (3.51°), $Mg_{21}Zn_{25}$ (3.61°), Mg_4Zn_7 (3.66°) and $MgZn_2$ (3.73°), develop at the expense of the Zn peaks. Finally, in interface III region, the Zn peaks are hardly detected, implying the almost complete disappearance of Zn. Although no Mg-Zn IMCs are detected by microstructural observation, Fig. 8**(d)**, the $Mg_{51}Zn_{20}$ and $Mg_{21}Zn_{25}$ reflections are indexed by diffraction analysis, see

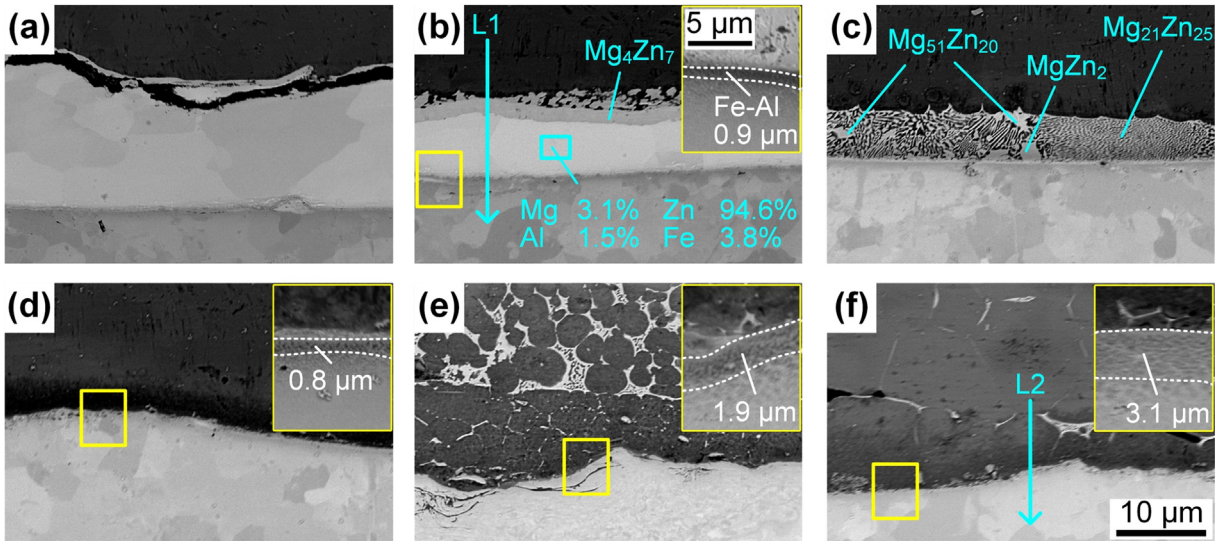

Fig. 8. Analysis of interfacial microstructure of the H-weld: (a) interface I, (b) interface II-1, (c) interface II-2, (d) interface III and (e) interface IV-1, x = 3.0 mm, (f) interface IV-2, x = 1.0 mm, regions. The higher magnificated images, indicated by the yellow squares, are embedded on the corner of each figure. (For interpretation of the references to colour in this figure legend, the reader is referred to the web version of this article.)

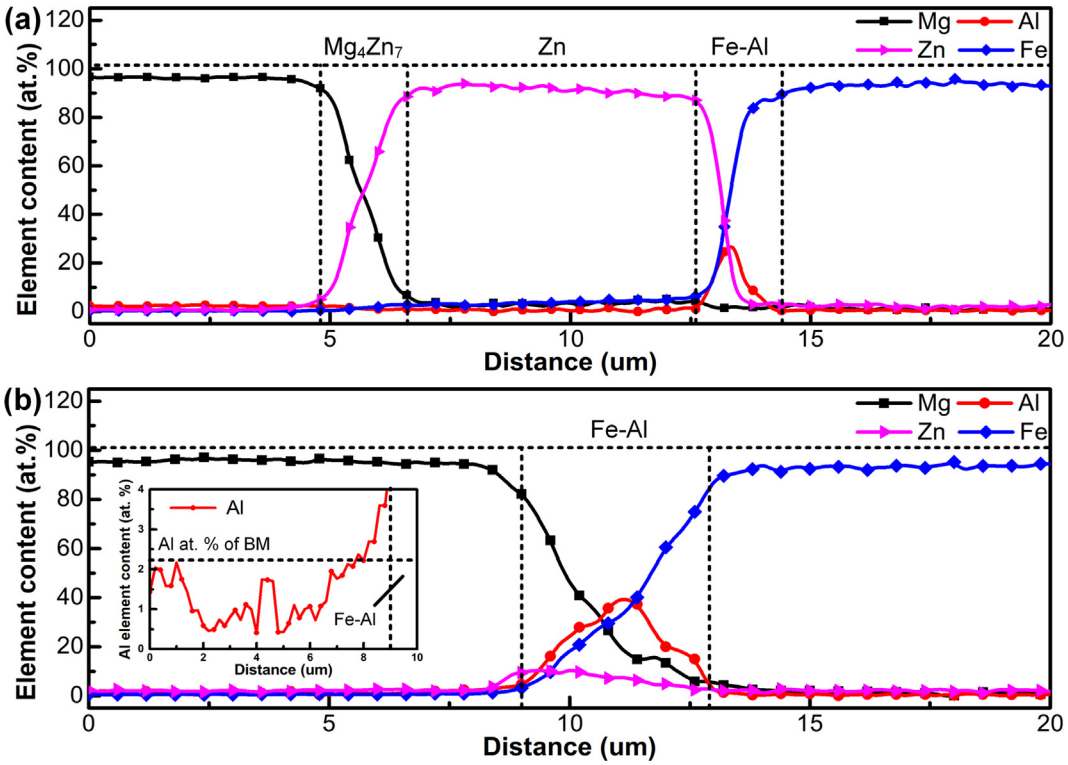

Fig. 9. EDS line scan results across (a) the interface II-1 (L1, illustrated in Fig. 8(b)), and (b) the interface IV-2(L2, Fig. 8(f)) of the H-weld, the embedded figure shows the detailed variation of Al close to the Fe-Al reaction layer.

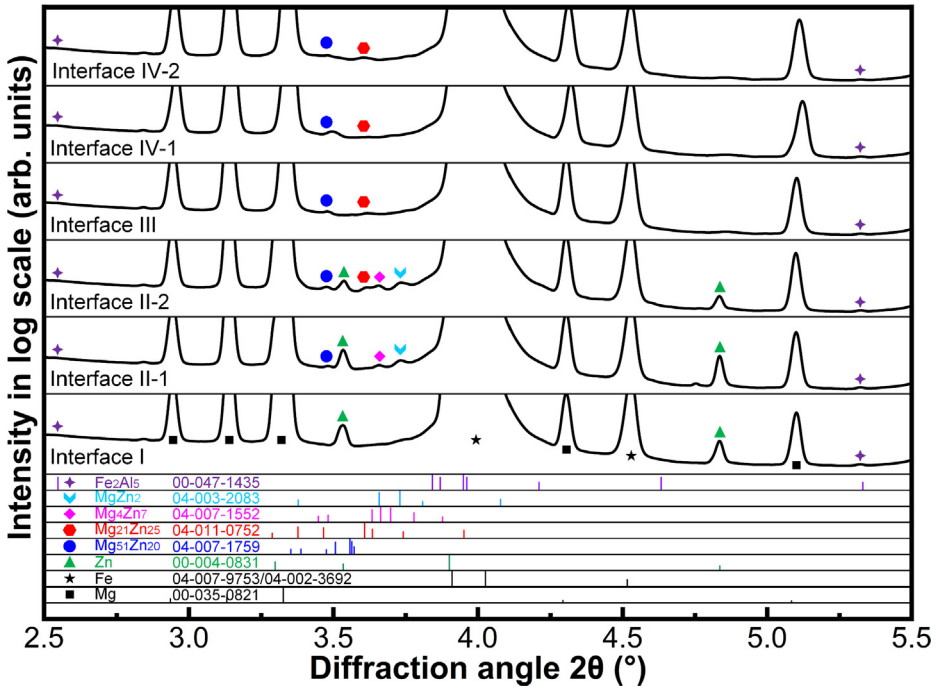

Fig. 10. Indexed HEXRD diffractograms of interfacial regions. The corresponding positions of Bragg peaks, which are calculated according to referred PDFs numbers of ICDD, are also indicated.

Fig. 10. The interface IV-1 and IV-2 regions are featured with the similar patterns as that of interface III. Additionally, it should be noticed that the Fe_2Al_5 is identified at 2.13° and 5.33° along the whole interface, suggesting that the phase in Fe-Al layer, shown in Fig. 8, is Fe_2Al_5.

As far as the L-weld is concerned, Fig. 11, compared with the H-weld, some differences exist. Firstly, the width of the identified interface II region is only two-third of that in the H-weld, and the interface III region is hardly observed. Secondly, in the interface II region, although extrusion of Mg-Zn eutectic is observed and the

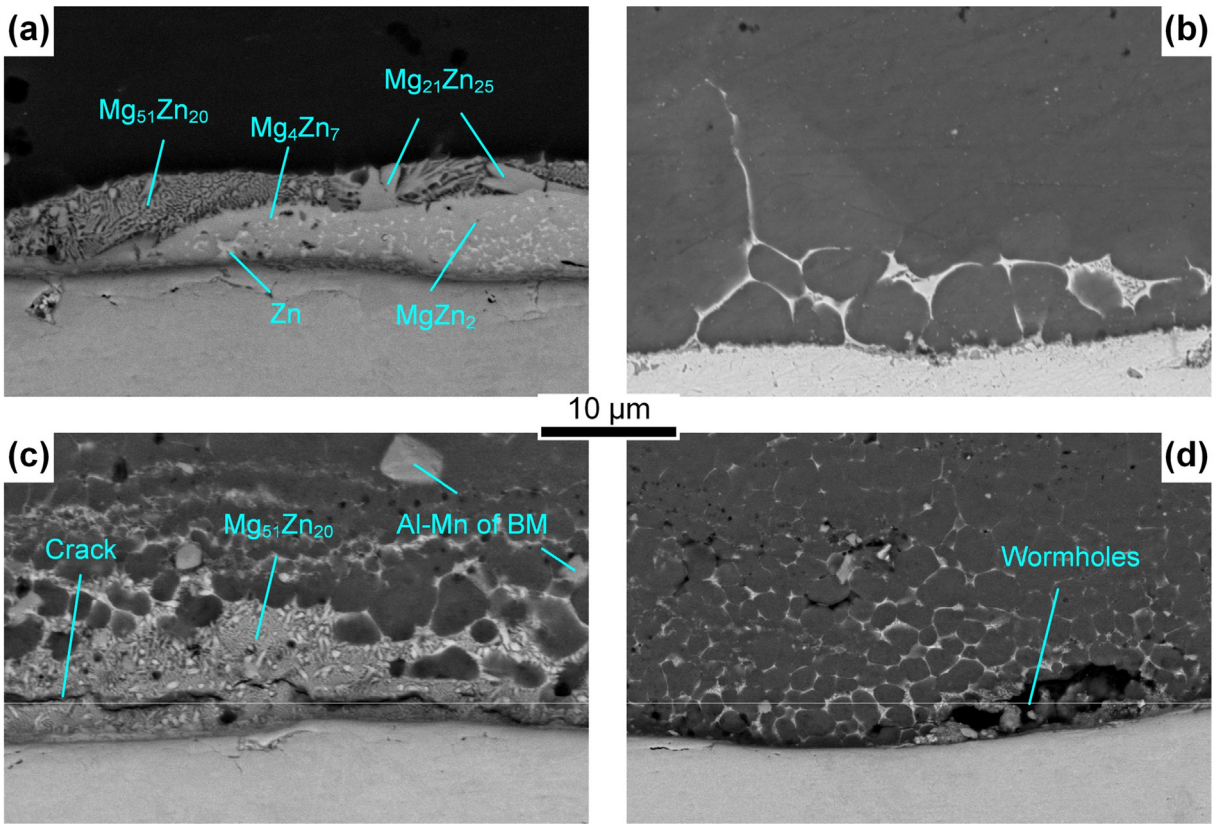

Fig. 11. Analysis of interfacial microstructure of the L-weld: (a) interface II-1, (b) interface II-2, (c) interface IV-1, x = 3.0 mm and (d) interface IV-2, x = 0 mm, regions.

Mg-Zn IMCs with different compositions are detected, Fig. 11**(a)**, the amount of Mg-Zn eutectics significantly decreased, Fig. 11**(b)**. Thirdly, for the Mg-Zn eutectics in interface IV region, instead of being moved away from the interface as in the H-weld, in the L-weld, large amounts of Mg-Zn eutectics are spread along the interface, Fig. 11**(c)**, and flaws such as cracks, wormholes are present, Fig. 11**(d)**. Lastly, in all the interfacial regions, the thickness of Fe-Al layer is below 1 μm, thus a growth behavior has not emerged. For completeness, the microstructural features of the interfacial regions for the L-weld are summarized in Supplementary **Table S5**.

The differences in the interfacial structures between H-weld and L-weld will affect the mechanical properties of the weld, which is discussed in the following section.

3.3. Mechanical properties

3.3.1. Deformation and fracture behavior in LSS test

To better understand the underlying mechanism of failure and its relationship with the interfacial structure, the deformation of the weld during LSS tests was monitored. However, due to the geometrical characteristic of the spot joint connection, a direct observation of the interfacial region is impossible. Considering the integrality of the joint, the deformation of the interfacial regions will be reflected on the sheet surface [56], and in general, the strain concentration on the surface implies the formation of internal cracks in position along the sheet thickness direction [57,58]. Thus, the deformation of the Mg sheet upper surface was investigated via DIC from which an equivalent strain measure, i.e. von Mises strain, was calculated at different loading stages, i.e. 60%-100% maximum LSS, as shown in Figs. 12 and 13.

For the H-weld, Fig. 12, strain localization occurs with increase of lap shear force in the regions outside the SZ but also within the SZ, in particular at the transition from clamping ring to shoulder, Fig. 12**(a)**. Additionally, it is interesting to see that, on the two sides of the Mg specimen, i.e. loaded side and free side, Fig. 2**(a)**, the distribution of the strain field is asymmetric, which is related to the configuration of the weld. During lap shear test, for the upper Mg sheet, the loaded side experiences tensile stresses along the interface, while the free side is under the effect of compressive stresses [36,59]. Therefore, cracks first occur on the loaded side, resulting in higher overall strains than the free side. The strain asymmetry is further clearly shown in the detailed strain distribution along the z-axis, Fig. 12**(b)**. On the loaded side, strain in all the interfacial regions increases locally with increasing force, thus the entire Mg-steel interface contributes to the strength.

In the case of the L-weld, strain field is shown in Fig. 13**(a)**, in the early stages of deformation, strain localization occurs only in the outer regions of the SZ. When the maximum force is reached, the strain localizes slightly into the shoulder refill region. The strain distribution along z-axis, shown in Fig. 13**(b)**, illustrates that only the strains in interfaces I and II significantly increase with applied force, while most of the interface IV does not contribute to the deformation. During LSS test, cracks mainly form and extend around the interface I and II. Once the cracks propagate into the interface IV, the complete failure happens very quickly, as a result, the strain variation in interface IV cannot be captured by the DIC anymore, even if a high frame rate is used during the measurement.

In addition, the comparison of the strain distribution at maximum LSS of the L-weld and 60% maximum LSS of the H-weld, Fig. 12**(b) and 13(b)**, representing approximately the application of similar forces, shows that the strain, in particular in the interface II region of the L-weld is significantly higher than in the H-weld. This is related to the decreased Mg-Zn eutectics in the interface II region of the L-weld, Fig. 11**(b)**, which results in a reduced bonding strength.

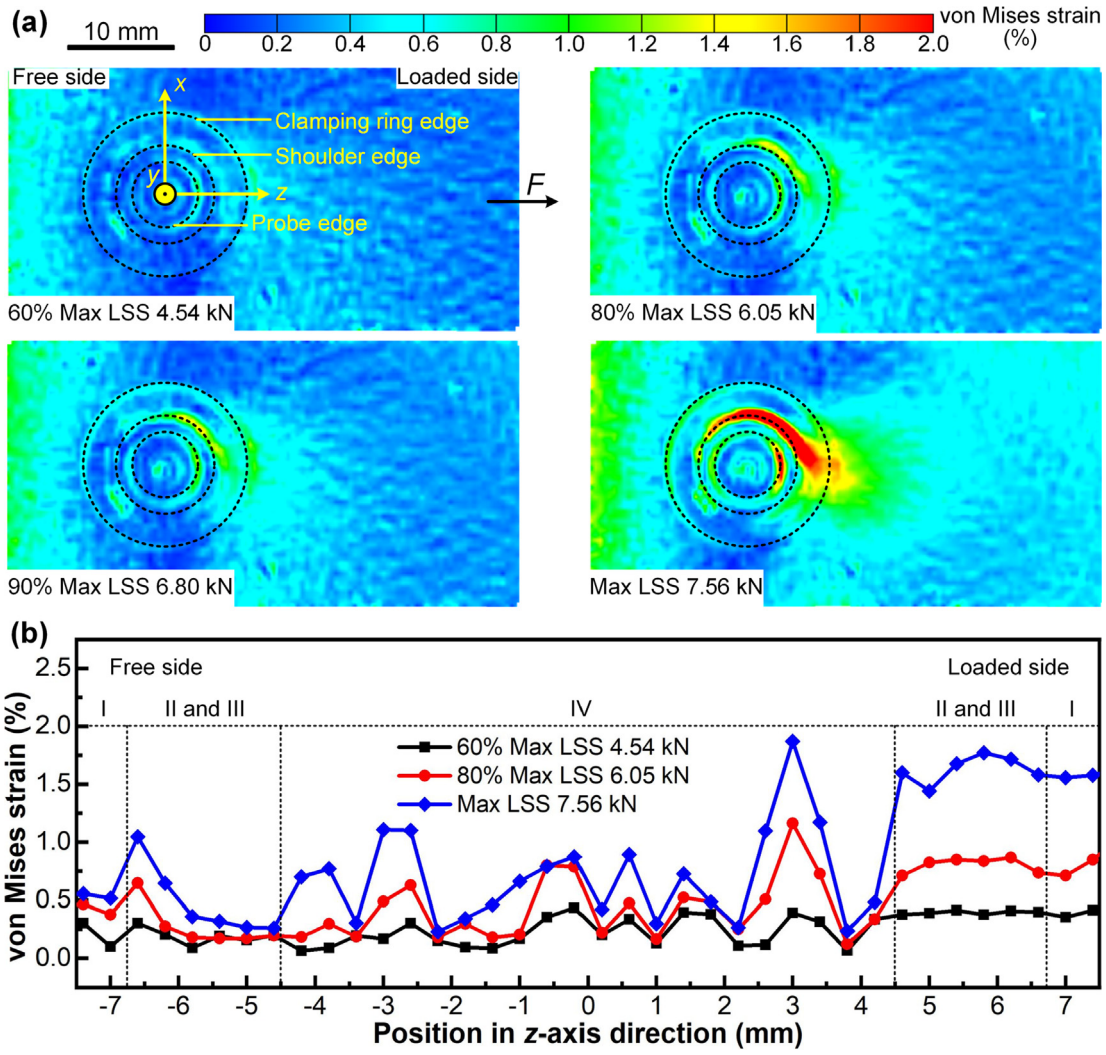

Fig. 12. Analysis of the strain distribution during lap shear test for the H-weld. (a) von Mises strain field determined for the Mg sheet upper surface at different stages. (b) von Mises strain profile along *z*-axis at different stages, the corresponding interfacial regions are also illustrated.

The differences in the sheet deformation behavior between H-weld and L-weld inevitably affect the fracture behavior. Fig. 14 **(a)** presents the fractography of the H-weld on the Mg side, whereby the fracture position and its relationship with the interfacial regions are also illustrated. High magnification images of the free side and loaded side captured by backscatter electron signal are shown in Fig. 14**(b) and (c)**, respectively. During lap shear test, the cracks extend along the complex path, thus the fracture surface shows complicated features. The chemical composition analysis via EDS is conducted in different regions to identify the featured phases. For the interface I regions on both free and loaded sides, cracks propagate along the interface of Mg and Zn coating. Some broken Zn phases bond can be observed on the Mg side. In contrast, in the interface II region, the cracks propagate mainly along the Mg-Zn eutectics. When the cracks reach interface III region, failure occurs on the interface of Mg and steel. Although the interfacial structure of the *y*-*z* cross-section is not reported here, it is important to note that the interface III region is not present on the free side, which is related to the difference in cooling condition on both sides. Mg has a higher heat conductivity than steel, thus better cooling condition exists on the loaded side due to the increased contact area with Mg alloy. Compared to the free side, the decreased amount of liquid Mg-Zn is squeezed out on the loaded side at a limited distance, as a result, the width of interface II region decreases and the interface III region without solidified Mg-Zn IMCs forms. In the interface IV region on the free side, failure occurs along the Fe-Al IMC layer and Mg SZ, Fig. 14**(d)**, while on the loaded side, as near to the SZ center, failure extends initially across Mg-Zn eutectics, Fig. 14**(e)**, and then propagates into the Fe-Al IMCs layer and Mg matrix of SZ in sequence.

The fractographic analysis of the Mg surface of the L-weld is illustrated in Fig. 15. In the interface II region, the cracks firstly extend across Mg-Zn eutectics and then grow along Mg/steel interface due to the decreased amount of Mg-Zn eutectics in interface II-2 region, Fig. 11**(b)**. Unlike the H-weld, no Fe-Al IMCs are observed on the fracture surface within interface IV region in the L-weld, while the Mg-Zn eutectics are frequently identified, which are usually accompanied by cracks associated with local melting, Fig. 15**(d)**, or brittleness of Mg-Zn IMCs, Fig. 15**(e)**. The flaws present along the interface IV of L-weld, Fig. 11**(c) and (d)**, offer favorable paths for crack propagation during the LSS test.

3.3.2. Microhardness

Fig. 16 presents the microhardness distributions on the Mg side of the H-weld and L-weld. For the H-weld, Fig. 16**(a)**, three characteristic regions can be identified. Regions with microhardness values between 60 $HV_{0.1}$ and 70 $HV_{0.1}$ within the SZ are identified as the Mg matrix. Due to the refined grains resulted from recrystal-

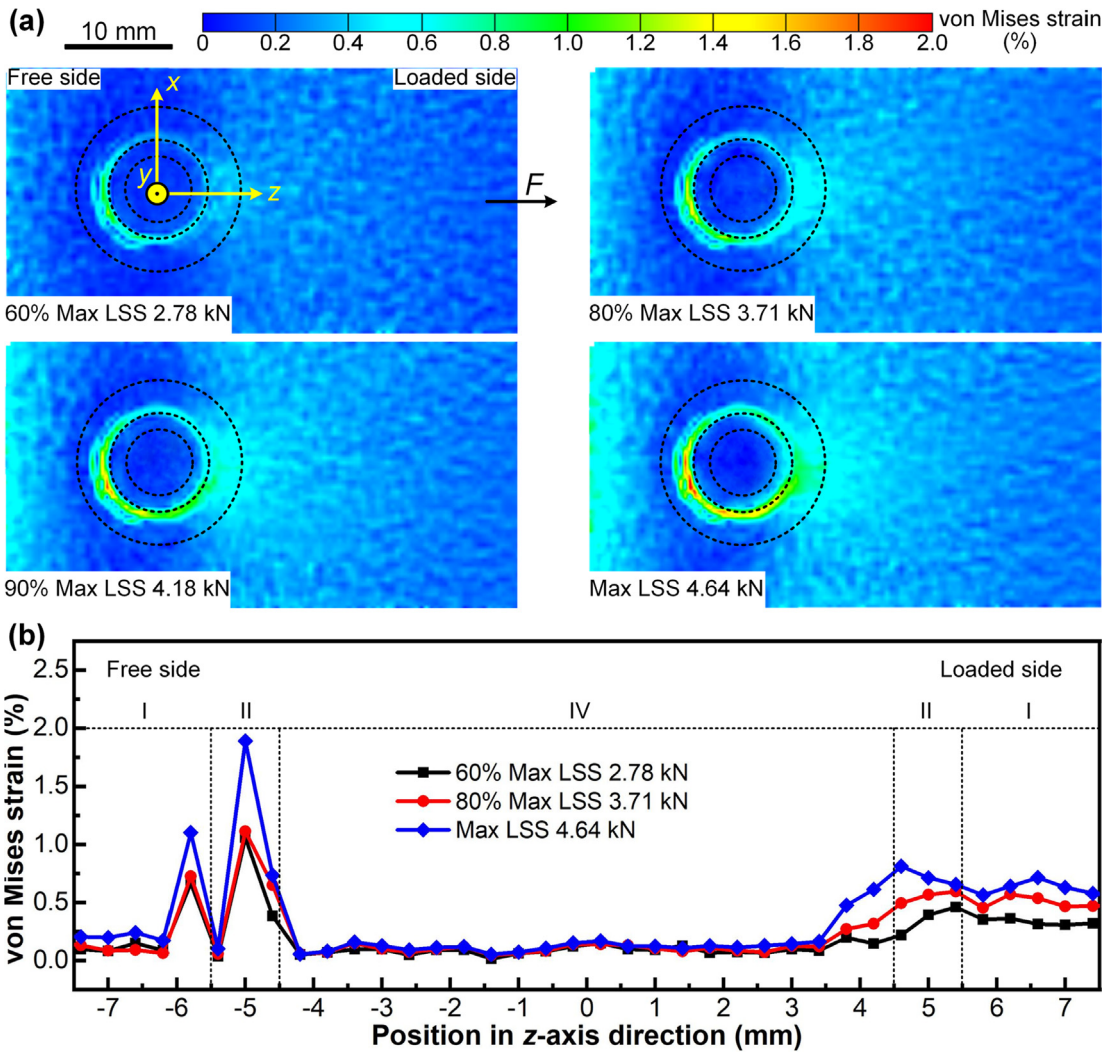

Fig. 13. Analysis of the strain distribution during lap shear test for the L-weld, (a) von Mises strain field determined for the Mg sheet upper surface at different stages. (b) von Mises strain profile along *z*-axis at different stages, the corresponding interfacial regions are also illustrated. No interface III region is present in the L-weld.

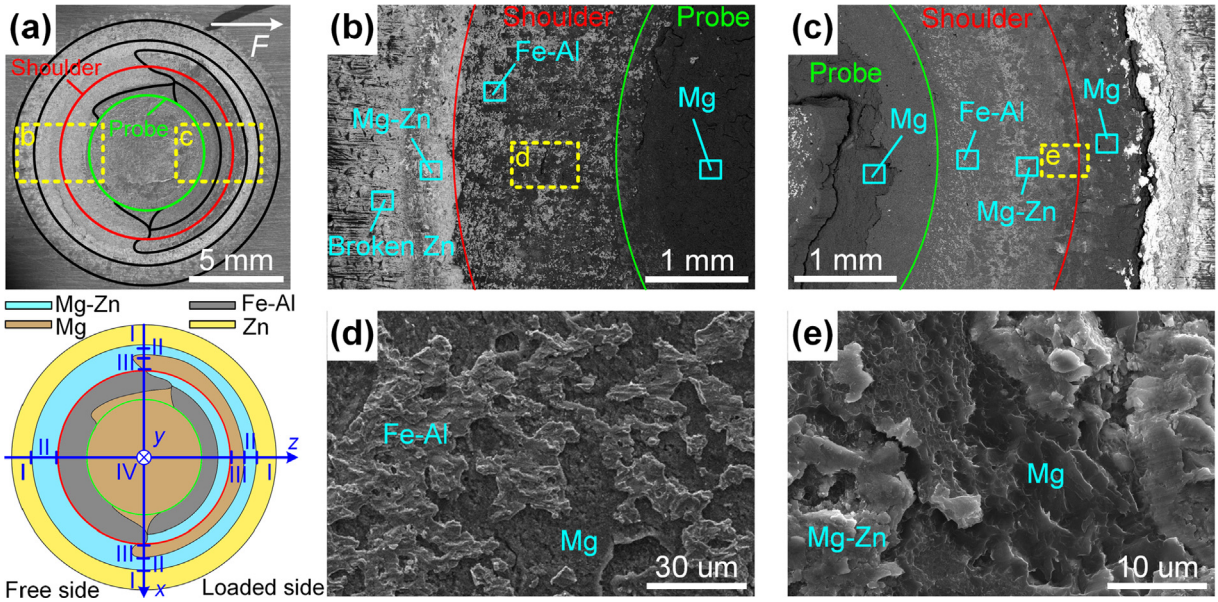

Fig. 14. Fractographic analysis of the H-weld. (a) Fracture surface of Mg side and illustration of fracture position. (b-e) Details of marked regions in fracture surface.

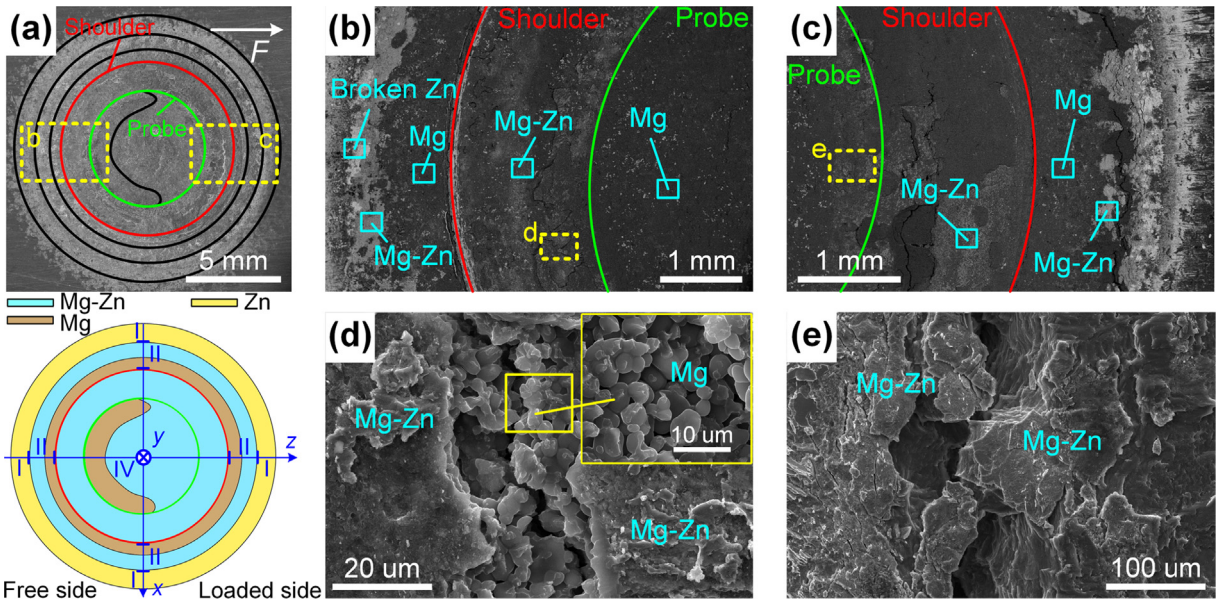

Fig. 15. Fractographic analysis of the L-weld. (a) Fracture surface of Mg side and illustration of fracture position. (b-e) Details of marked regions in fracture surface.

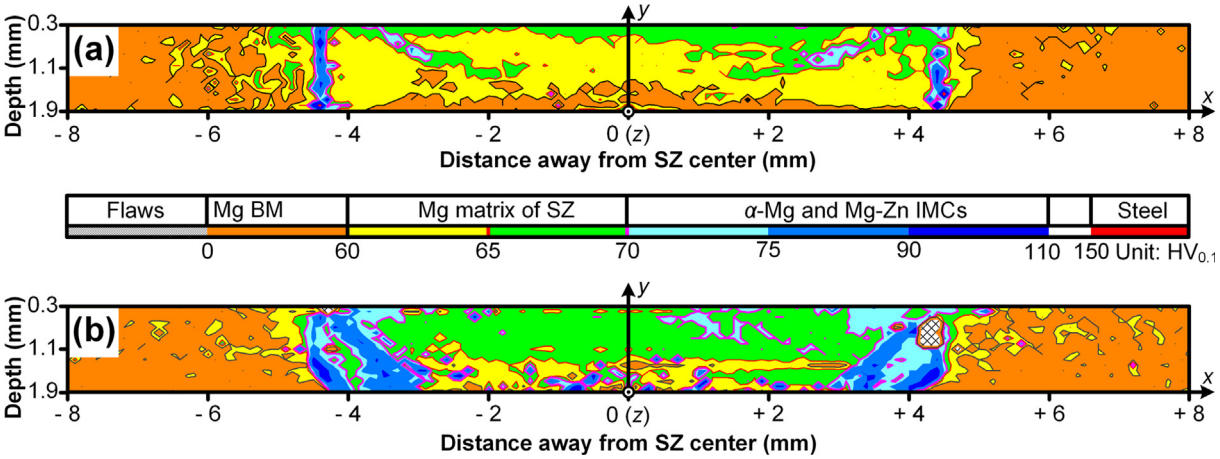

Fig. 16. Microhardness profiles of the Mg side in the (a) H-weld and (b) L-weld.

lization, the microhardness is higher compared to the BM. The bright regions composed of α-Mg and Mg-Zn IMCs observed in the microstructural investigation show a further increased microhardness, i.e. 70–110 $HV_{0.1}$, which is related to the effect of solid solution strengthening and the formation of IMCs. In addition, some regions exhibit a microhardness above 150 $HV_{0.1}$, where the presence of small steel fragments transported into the SZ by material flow are assumed to contribute to such a high microhardness. In the L-weld, Fig. 16**(b)**, Mg matrix of SZ and Mg-Zn eutectics have been identified as well as regions containing flaws. Compared to the H-weld, the area in the shoulder refill zone and near the Mg/steel interface within SZ of L-weld show a microhardness above 70 $HV_{0.1}$ due to the increased presence of Mg-Zn eutectics.

4. Discussions

4.1. Liquation

Although refill FSSW is considered as a solid state welding process, in the Mg/galvanized steel weld, Mg-Zn eutectics with solidification microstructure have been observed, implying the occurrence of liquation during welding. Liquation was also observed in the refill FSSW of Al/Mg [37], Al/Cu [39] and Al/galvanized steel [40,60]. It is reported that under the combined effects of high-temperature exposure and the enhanced mutual diffusion from severe plastic deformation [39], the local chemical composition of the weld could reach the eutectic composition (Al-Mg, Al-Cu or Al-Zn), resulting in the formation of liquid phases [37,61]. Liquation will bring some specific features to the refill FSSW of Mg/galvanized steel compared to Mg/Mg similar and Mg/bare steel dissimilar welds. These features are significantly reflected in the thermal cycles, as shown in Fig. 17.

Fig. 17**(a)** shows the thermal cycles obtained by thermocouples at × = 0 (center of welds) and × = 6 mm for the H-weld. For comparison purpose, the temperature variations for refill FSSW of similar Mg/Mg as well as dissimilar Mg/bare steel combinations, welded with the same process parameters are also displayed.

For the Mg/Mg and Mg/bare steel welds, the temperature increases steadily during the plunge and dwell stage and decreases from about 0.3 s after the beginning of retraction stage. While for Mg/galvanized steel weld, the temperature firstly increases quickly during plunge stage until reaching the melting point of pure Zn

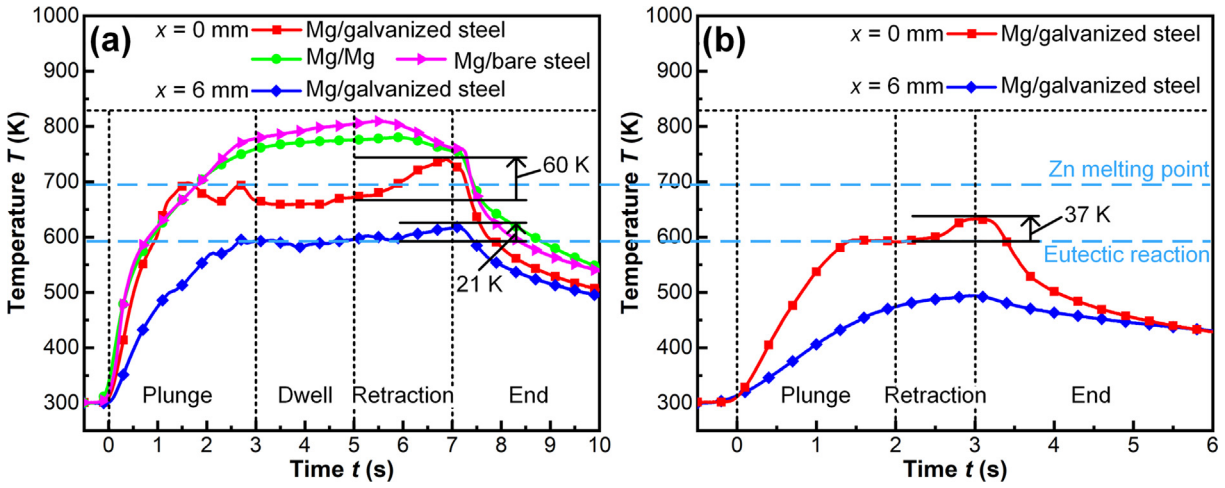

Fig. 17. Thermal cycles of the (a) H-weld, the results of Mg/Mg and Mg/bare steel welds at × = 0 with the same parameters are also given, and (b) L-weld. The welding process finishes at the end of the retraction stage.

(692 K). Afterwards, the temperature decreases slightly to 660 K. Such variation of the temperature repeats and subsequently, during dwell stage, the temperature is nearly stationary and only fluctuates between 650 K – 680 K. Finally, from the beginning of retraction stage, the temperature unexpectedly raises to about 60 K instead of declining such as in Mg/Mg or Mg/bare steel cases. Overall, the maximum temperature reached during the Mg/galvanized steel weld is lower than that during the Mg/Mg (780 K) and Mg/bare St (809 K) welds. The similar temperature variation is also observed at × = 6 mm position, where the temperature increases to the Mg-Zn eutectic reaction temperature first and then keeps near this temperature during the plunge stage. From the time of about 0.3 s after the beginning of retraction stage, the unexpected temperature increase by around 21 K is identified.

The different thermal cycle in the Mg/galvanized steel weld compared to the Mg/Mg and the Mg/bare steel combinations is related to liquation. As in FSW [62], the heat generation in refill FSSW is composed of three parts: (i) the friction heat E_f at the shoulder/probe-workpiece interface due to the partial stick–slip condition, (ii) the plastic dissipation E_d of the material and (iii) the viscous dissipation E_v originated from deformation energy stored within the plastic material. For the × = 0 mm position in the H-weld, during welding, when the temperature reaches the melting point of Zn, the Zn-coating starts to melt, resulting in the formation of a liquid film distributed at the tool-workpiece interface and at the grain boundaries of plastic material, i.e. incipient melting. The liquid film acts as "lubricant", causing tool slippage and decreasing torque and strain rate. Thus, the produced heat reduces, which leads to a reduction of the temperature below the Zn melting point. Once the liquid Zn has solidified, the heat input increase again, resulting in subsequent temperature increase to the Zn melting point. The liquidus temperature of the Zn eutectic compound decreases due to dissolved Mg and Al elements [60]. Furthermore, apart from Zn, the eutectic reaction between Mg and Zn also contributes to liquation. With increasing presence of a liquid phase, a "self-adjusting" condition [37] of heat generation and dissipation is finally reached, i.e. the temperature remains unchanged between Mg-Zn eutectic reaction temperature and liquidus temperature of molten Zn. For the position near to the interface II region, i.e. at × = 6 mm, liquid Mg-Zn eutectics are squeezed from the SZ to this region, Fig. 8**(c)**, so that the temperature remains at the eutectic reaction temperature.

During the retraction stage, the heat generation near the interface decreases due to the retraction of the tool. Thus, for the Mg/Mg and Mg/bare steel welds, the temperature measured decreases. However, the unexpected increase in temperature is identified for the Mg/galvanized steel refill FSSW procedure. An assumption is that the solidification of liquid phases (mainly liquid Mg-Zn eutectics) may happen, which is an exothermic reaction, offering additional heat to increase the temperature along the Mg/steel interface. According to the microstructure observation, Fig. 4**(a)**, it is estimated that about 1×10^{-4} mol Zn (a columnar region with the diameter of 6.7 mm and thickness of 9.7 μm, 0.01 g) reacts with Mg during welding. Based on the data measured by Berch et al. [63], the solidification of liquid Mg-Zn can only provide maximum heat of 2 J. As a comparison, the heat produced by refill FSSW of H-welds is above 6 kJ, as calculated in Supplementary **Table S6**. Thus, the heat generation due to the solidification of liquid phases is negligible, which is not the possible reason for the increased temperature. In fact, during retraction stage, the increased amounts of liquid phases are transported away from the interfacial region with material flow. The lubricant effect of liquid phases is reduced, resulting in the disappearance of "self-adjusting" state, i.e., more heat is generated locally, thus the temperature along Mg/steel interface increases steadily until the end of refill FSSW. The varied distribution of liquid phases will be discussed in detail in Section 4.2 to reveal the underlying joining mechanism.

In case of L-weld, liquid Mg-Zn eutectics accumulate along the Mg/steel interface, Fig. 11**(c) and (d)**, thus the temperature in the SZ stabilizes at the Mg-Zn eutectic reaction temperature during refill FSSW, Fig. 17**(b)**, and the unexpected increase of temperature, resulted from the decreased amount of liquid phases along Mg/steel interface due to material flow as described before, is observed as well. At × = 6 mm position, unlike H-weld, the maximum temperature is much lower than the Mg-Zn eutectic reaction temperature, corresponding to the observation that the width of interface II region of L-weld is reduced compared to H-weld, as shown in Fig. 4**(a) and (b)**.

4.2. Joining mechanism

Based on the results and the discussion on the liquation phenomenon, the joining mechanism of refill FSSW of Mg to galvanized steel can be proposed. Additionally, the material flow, which is a key to understanding the involved physical process in refill FSSW [31,64,65], cannot be omitted when revealing the underlying mechanism. According to the macro/microstructure observation by BSE signal, the material flow behavior can be

reflected by the transportation and deposition of Mg-Zn phases, which show the lighter contrast compared to Mg matrix, Figs. 4 and 6. The "stop-action" technique [31,66] was carried out to trace the distribution of Mg-Zn phases during refill FSSW to infer the variation of material flow. In the stop-action experiments, the welding process was interrupted in plunge stage at specific depths, i.e., 1.8 mm for H-welds and 1.5 mm for L-welds, as well as during retraction stage at the depth 1.5 mm for both cases. A water–ice mixture was then immediately poured on the welding region to "freeze" the macro/microstructure.

The schematic illustration of the welding procedure for H-weld conditions is shown in Fig. 18, the distribution of Mg-Zn, as well as the established material flow direction of each local region according to stop-action, are also marked. Before welding, Fig. 18**(a)**, regardless of surface preparation (degreasing in the present study), small amounts of oxides and contaminants remain on the sheet surfaces, and a given clearance exists between Mg and steel. In the plunge stage, Fig. 18**(b)**, the interaction between material and tool leads to severe plastic deformation and heat generation within the materials, the oxide layer is broken and the original Zn coating melts. The liquid Zn dissolves Mg, subsequently the liquid Mg-Zn phases of different compositions are formed. Due to the material flow introduced by tool plunge, shown as white arrows in Fig. 18 **(b)**, some molten Mg-Zn is transported into the SZ, which then agglomerates along the interface between shoulder and SZ under the effect of shear obtained by tool rotation. The tool slippage occurs, and the "self-adjusting" temperature cycle, Fig. 17**(a)**, is achieved. Additionally, most molten Mg-Zn with broken oxides and contaminants are squeezed far away from the SZ to fill the clearance between Mg and steel. Due to the dissolution of the Zn coating, the direct contact of the fresh steel surface with recrystallized Mg occurs. Al present in the Mg alloy segregates preferentially near the Mg/steel interface due to the chemical potential difference and interacts with the original Fe-Al IMCs layer and Fe. The original Fe-Al layer acts as a nucleation site and the formation and growth of the new Fe-Al layer occur, which are associated with atom diffusion and favorable for the metallurgical bonding between Mg and steel. Since Al atoms have a higher diffusion rate in Fe-Al IMCs than the Fe atoms [67], the formation and growth of the new Fe-Al layer are mainly controlled by Al and its growth direction is towards the steel side, as shown in the embedded enlarged image of the interfacial region marked in Fig. 18**(b)**. In the following dwell and retraction stages, Fig. 18**(c)**, the thickness of the Fe-Al layer increases, and the liquid Mg-Zn is further pushed towards the SZ-shoulder interface or out from the SZ under the combined effects of tool translational movement and rotation. It should be noticed that, according to the results of stop-action experiment in the retraction stage, with the progress of welding, the amount of liquid Mg-Zn phases adjacent to the Mg/steel interface decreases as expected, which verifies the above analysis that the abnormal increase in temperature, shown in Fig. 17, is related to the local loss of "self-adjusting". After welding, Fig. 18**(d)**, the liquid phases solidify, bright regions composed of α-Mg and Mg-Zn IMCs form in the SZ, Fig. 6, while along the interface, different interfacial regions with characteristic microstructures are formed, shown in Fig. 8.

The joint formation procedure for the Mg/galvanized steel in the L-weld is characterized by radically different phenomena. In the plunge stage, Fig. 19**(b)**, the temperature measured by the thermocouple in the center of the weld is much lower than the Zn melting point and is kept near the Mg-Zn eutectic temperature, Fig. 17**(b)**. Thus, the disappearance of original Zn coating is a gradual process due to Mg-Zn chemical reaction instead of direct melting as seen for the H-weld. Additionally, unlike the distribution of Mg-Zn liquid phases in H-weld, in which large amount of Mg-Zn is squeezed out of the SZ, they only accumulate near the Mg/steel interface instead. In the following retraction stage, Fig. 19**(c)**, although the squeeze-out phenomenon of Mg-Zn liquid phases is identified, they still mainly spread along the interface, and with the retraction movement of shoulder, increased amount of Mg-Zn is transported into the shoulder refill region of SZ. For the L-weld, on one hand, the molten Mg-Zn along the interface restrain the contact of the original Fe-Al layer with Mg, the growth of the Fe-Al layer is suppressed. On the other hand, during the solidification of the liquid Mg-Zn, flaws such as cracks and voids appear near the interface, as shown in Fig. 11**(c) and (d) and 19(d)**. Thus, the bonding strength of interface IV decreases significantly. For the interface II, which also contributes to the strength of the weld, due to the low plunge depth, see process parameters used for the L-weld, only limited amount of liquid Mg-Zn is squeezed out of the SZ, as indicated in Fig. 19**(b) and (c)**, the width of interface II decreases and the bonding strength is also weakened. Finally, low LSS is obtained for the L-weld.

The comparison of joint formation phenomena between H-weld and L-weld described above clarifies the importance of two factors to achieve high-quality bonding between Mg and steel by refill FSSW:

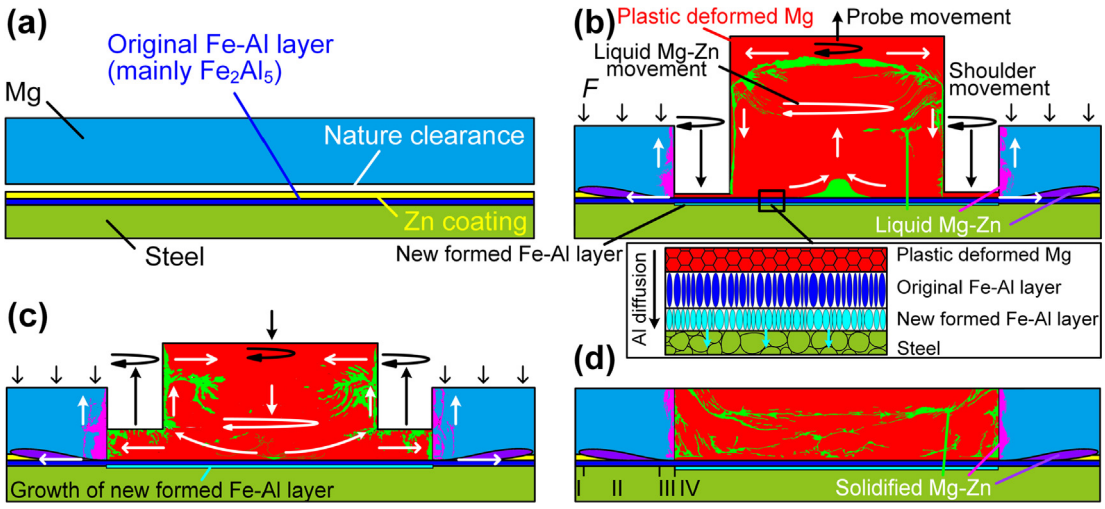

Fig. 18. Illustration of the welding procedure in refill FSSW for the H-weld conditions: (a) before welding; (b) plunge stage; (c) retraction stage and (d) after welding. The distribution of Mg-Zn in plunge and retraction stages is obtained by "stop-action", the material flow direction of each local regions is marked by white arrow.

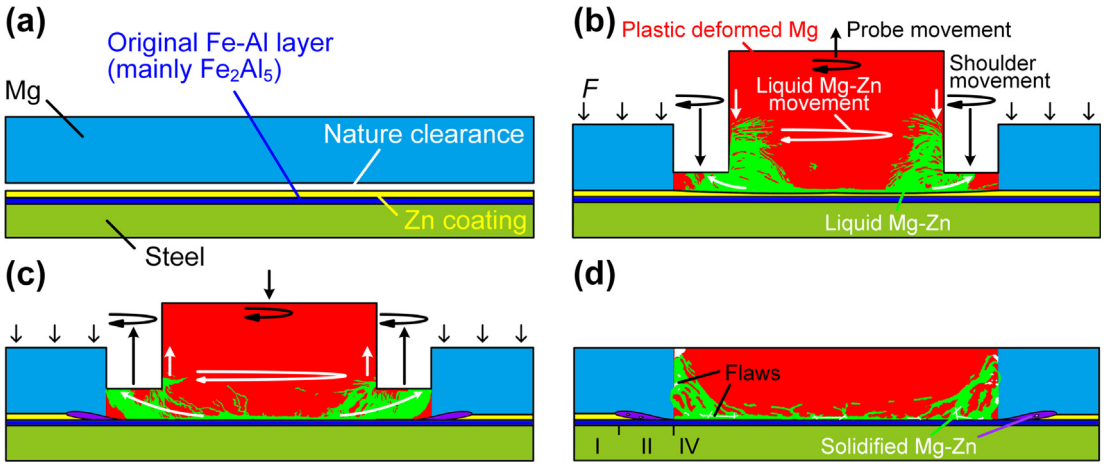

Fig. 19. Illustration of the welding procedure in refill FSSW for the L-weld conditions: (a) before welding; (b) plunge stage; (c) retraction stage and (d) after welding.

(1) the Zn coating. On one hand, the Zn coating offers a protection function, the squeezed liquid Mg-Zn could remove the oxides and mechanically seal the SZ to protect the Mg/steel interface from oxidation. On the other hand, the Zn coating behaves as brazing filler between Mg and steel in the interface II region. As a result, Mg and steel are welded by the Mg-Zn reaction layer composed of Mg-Zn eutectics and IMCs, Fig. 8**(b) and (c)**. In contrast, in the refill FSSW of Mg/bare steel, welded with the same process parameters, the LSS of the weld is less than 2.0 kN and large amounts of Mg oxides are observed on the fracture surface, Fig. 20 **(a)**. There are no significant traces of welding between Mg and steel. It seems that Mg and the bare steel are jointed mainly by adhesion and mechanical interlocking, thus the Zn coating is beneficial for the welding between Mg and steel. The importance of Zn has also been reported in other welding processes [5,12,13,27], but its main functions are different, for example, in laser-brazing of Mg to galvanized steel [13], Zn coating acted to promote the wetting and spreading of liquid filler on the Mg/steel interface.

(2) the Fe-Al layer and its growth. The reaction of Al present in the Mg alloy with Fe results in growth of the original Fe-Al layer, which contributes to the joining by diffusion in the interface IV region. According to the edge-to-edge matching model [68], the lattice mismatching of Mg hexagonal close-packed (HCP) crystal structure and Fe body-centered cubic (BCC) structure is very large. High interfacial energy density exists between Mg and Fe and the Mg/Fe interface is the weakest position. In refill FSSW of Mg to galvanized steel, the Fe-Al layer is mainly composed of orthorhombic Fe_2Al_5, which acts as the transition layer in interface IV region, Fig. 8**(e) and (f)**. For the Fe_2Al_5/Mg interface, a good lattice matching is obtained with the orientation relationships (ORs) $[0\bar{1}0]_{Fe2Al5}$ // $[100]_{Mg}$ and $(002)_{Fe2Al5}$ // $(01\bar{1}\,\bar{2})_{Mg}$, while for the Fe/$Fe_2Al_5$ interface, the ORs are $[10]\bar{1}_{Fe2Al5}$ // $[11]\bar{1}_{Fe}$ and $(002)_{Fe2Al5}$ // $(110)_{Fe}$ [69], thus the low energy density of Mg/Fe_2Al_5/Fe interfaces is obtained, resulting in an improved metallurgical bonding between Mg and Fe. With the increase in Fe-Al layer thickness, the bonding strength of Mg/Fe_2Al_5/Fe increases, and in lap shear test, cracks extend across the Mg SZ in the probe refill region, Fig. 14**(a)**. In a previous study on FSSW of AZ31 Mg alloy to galvanized steel, Xu et al. [29] also reported that the Fe-Al layer was beneficial for the bonding between Mg and steel, and implied that the growth of the Fe-Al layer resulted from the reaction between Al element in the Zn coating with the steel substrate. However, in the case of refill FSSW, the

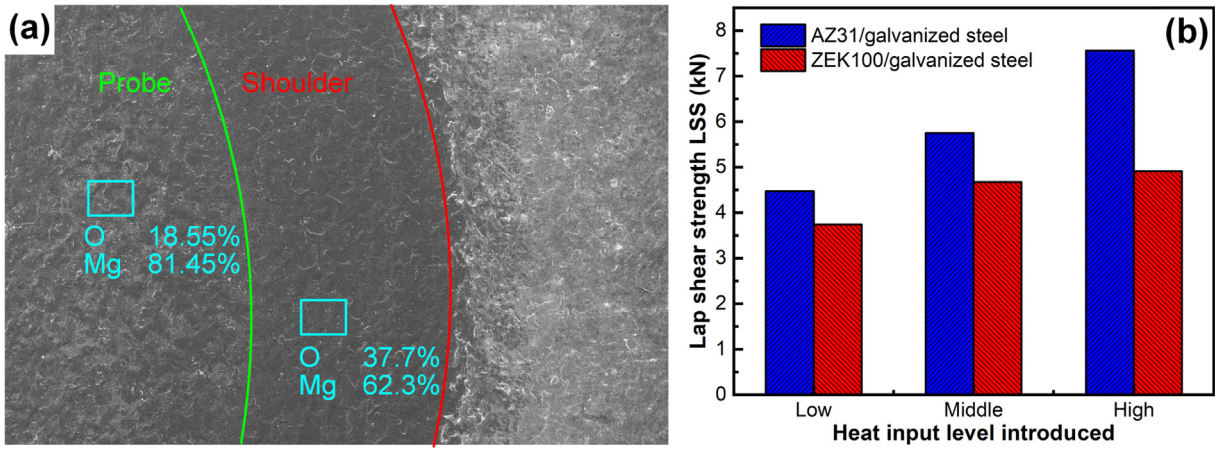

Fig. 20. (a) Fracture surface of Mg side in refill FSSW of AZ31B Mg to bare steel. (b) Comparison of the LSS between refill FSSW of AZ31/galvanized steel and ZEK100/galvanized steel for different parameter combinations, leading to different heat input (Low and high heat input levels are introduced by using parameter combinations of L-weld and H-weld, respectively. The parameters for the middle heat input are RS = 1600 rpm, PD = 1.8 mm, PT = 2 s, DT = 1 s, RT = 1 s).

significant growth of the Fe-Al layer in the interface IV region should be mainly related to the Al in the Mg BM. The Al content in the Zn coating is very low, not even being detected by the EDS analysis, as shown in Table 1, thus its effect on the growth of Fe-Al layer is assumed to be limited. In addition, according to the chemical composition analysis across the interface, Fig. 9**(b)**, the Al content near the Fe-Al interface is lower on the Mg side than that of the Mg BM, suggesting that the Al is consumed due to the growth of the Fe-Al layer. To further verify the effect of Al in the Mg BM, a short comparison study using the ZEK100 Mg alloy, which does not contain Al, was conducted. Although the same welding parameter combinations for both material combinations were used, the LSS of ZEK100 Mg/galvanized steel weld was always lower than the AZ31 Mg/galvanized steel weld, Fig. 20**(b)**, and the difference is more significant with increasing of heat input. The lower strength of the ZEK100 Mg/galvanized steel joint is related to the lack of growth of the Fe-Al layer since no Al is present in ZEK100 Mg.

According to the established joint formation procedure and the identified important roles of Zn coating and Al element, the joining mechanism in refill FSSW of Mg to galvanized steel can be concluded finally. The joining mechanism is a hybrid mechanism, which mainly includes brazing resulted from Zn and diffusion welding with the growth of Fe-Al IMCs layer along the interface.

5. Conclusions

In the present study, novel results of refill FSSW of AZ31 Mg to galvanized steel are reported. The microstructure of the weld is characterized, and the effect of the interfacial structure on the fracture behavior is described. Finally, the joining mechanism is elucidated. The following conclusions are drawn:

(1) Refill FSSW is a competitive welding method for welding of Mg to galvanized steel. Sound Mg/galvanized steel welds are obtained in a wide parameter combination range.
(2) Heterogeneous interfacial reactions occur along the Mg/steel interface, which can be divided into four regions. For the weld with high LSS, i.e. H-weld, no reactions between Mg and Zn coating are observed in interface I region. The interface II region is characterized by the formation of Mg-Zn eutectics and IMCs, and the original Zn coating is completely eliminated in interface III region. More importantly, in interface IV region, the growth of the original Fe-Al layer has been observed. However, for the weld with low LSS, i.e. L-weld, flaws such as cracks and voids were present in interface IV and the growth of the Fe-Al layer is not observed.
(3) During LSS tests, the whole Mg/steel interface contributes to the strength of the H-weld, from interface II to IV, failure extends across the Mg-Zn eutectics, Fe-Al layer and Mg SZ sequentially. For the L-weld, strain concentrations only occur in the regions outside the SZ. Flaws present in the interface IV within the SZ offer favorable paths for the propagation of failure.
(4) The Zn coating is beneficial for welding between Mg and steel, which protects the interface from oxidation and contributes to the joining between Mg and steel as brazing filler.
(5) The Fe-Al layer is vital for high-quality welding between Mg and steel. Al contained in the Mg alloy reacts with Fe, resulting in the growth of the Fe-Al layer, thus metallurgical bonding between Mg and steel is achieved, which is beneficial for the improvement of mechanical properties.
(6) The joining mechanism can be summarized as a hybrid mechanism including brazing resulted from Zn and diffusion welding from Fe-Al IMCs layer.

CRediT authorship contribution statement

Banglong Fu: Conceptualization, Methodology, Investigation, Visualization, Writing – original draft, Writing - review & editing. **Junjun Shen:** Conceptualization, Methodology, Supervision, Writing - review & editing. **Uceu F.H.R. Suhuddin:** Resources, Writing - review & editing, Supervision, Project administration. **Ayrton A. C. Pereira:** Investigation, Data curation, Writing - review & editing. **Emad Maawad:** Investigation, Data curation, Writing - review & editing. **Jorge F. Santos:** Conceptualization, Methodology, Writing - review & editing, Supervision, Project administration. **Benjamin Klusemann:** Writing - review & editing, Supervision, Project administration. **Michael Rethmeier:** Writing - review & editing, Supervision, Project administration.

Declaration of Competing Interest

The authors declare that they have no known competing financial interests or personal relationships that could have appeared to influence the work reported in this paper.

Acknowledgements

Banglong Fu is gratefully acknowledging the funding of China Scholarship Council (Grant No. 201506220158). The valuable suggestions from Ms. Changyun Sun (Ludwig-Maximilians-Universität München, LMU) are greatly appreciated. The authors are grateful to Prof. Dr. Norbert Hort and Daniel Strerath (Institute of Metallic Biomaterials, Helmholtz-Zentrum Hereon) for the help in determining the chemical compositions of BMs. We acknowledge Deutsches Elektronen-Synchrotron DESY (Hamburg, Germany), a member of the Helmholtz Association HGF, for the provision of experimental facilities. Parts of the research were carried out at the High Energy Materials Science (HEMS) of the Helmholtz-Zentrum Hereon using P07B beamline.

Data availability

All the raw/processed data required to reproduce these findings are available from the authors upon reasonable requests.

Appendix A. Supplementary material

Supplementary data to this article can be found online at https://doi.org/10.1016/j.matdes.2021.109997.

References

[1] C. Tan, L. Li, Y. Chen, W. Guo, Laser-tungsten inert gas hybrid welding of dissimilar metals AZ31B Mg alloys to Zn coated steel, Mater. Des. 49 (2013) 766–773, https://doi.org/10.1016/j.matdes.2013.02.049.
[2] M. Rethmeier, B. Kleinpeter, H. Wohlfahrt, MIG welding of magnesium alloys metallographic aspects, Weld. World. 48 (3-4) (2004) 28–33, https://doi.org/10.1007/BF03266424.
[3] T. Li, G. Song, P. Yu, et al., Interfacial microstructure evolution in fusion welding of immiscible Mg/Fe system, Mater. Des. 181 (2019), https://doi.org/10.1016/j.matdes.2019.107903.
[4] A. Nasiri, D. Weckman, Y. Zhou, Interfacial Microstructure of Laser Brazed AZ31B Magnesium to SnPlated Steel Sheet, Weld. J. (2015).
[5] S. Jana, Y. Hovanski, G.J. Grant, Friction stir lap welding of magnesium alloy to steel: a preliminary investigation, Metall. Mater. Trans. A. 41 (12) (2010) 3173–3182, https://doi.org/10.1007/s11661-010-0399-8.
[6] A. Sadeghi, J. Inoue, N. Kyokuta, T. Koseki, In situ deformation analysis of Mg in multilayer Mg-steel structures, Mater. Des. 119 (2017) 326–337, https://doi.org/10.1016/j.matdes.2017.01.078.

[7] Y.C. Chen, K. Nakata, Effect of surface states of steel on microstructure and mechanical properties of lap joints of magnesium alloy and steel by friction stir welding, Sci. Technol. Weld. Join. 15 (2010) 293–298, https://doi.org/10.1179/136217109X12568132624325.
[8] A.A. Nayeb-Hashemi, J.B. Clark, L.J. Swartzendruber, The Fe−Mg (Iron-Magnesium) system, Bull. Alloy Phase Diagr. 6 (1985) 235–238, https://doi.org/10.1007/BF02880405.
[9] P. Penner, L. Liu, A. Gerlich, et al., Dissimilar Resistance Spot Welding of Aluminum to Magnesium with ZnCoated Steel Interlayers, Weld. J. (2014).
[10] L. Li, C. Tan, Y. Chen, et al., Comparative study on microstructure and mechanical properties of laser welded–brazed Mg/mild steel and Mg/stainless steel joints, Mater. Des. 43 (2013) 59–65, https://doi.org/10.1016/j.matdes.2012.06.057.
[11] G. Song, S. Zhao, M.S. Khan, et al., Microscale bonding mechanism of Mg alloy and steel welded joint with nanoscale Al-based intermetallic compound interface layers, Mater. Today Commun. 26 (2021), https://doi.org/10.1016/j.mtcomm.2020.101924.
[12] C. Tan, B. Chen, X. Song, et al., Influence of Al Interlayer Thickness on Laser Welding of Mg/Steel, Weld J. 95 (2016) 384s–394s.
[13] L. Li, C. Tan, Y. Chen, et al., Influence of Zn Coating on Interfacial Reactions and Mechanical Properties During Laser Welding-Brazing of Mg to Steel, Metall. Mater. Trans. A. 43 (2012) 4740–4754, https://doi.org/10.1007/s11661-012-1266-6.
[14] R. Cao, J.H. Chang, Q. Huang, et al., Behaviors and effects of Zn coating on welding-brazing process of Al-Steel and Mg-steel dissimilar metals, J. Manuf. Process. 31 (2018) 674–688, https://doi.org/10.1016/j.jmapro.2018.01.001.
[15] G. Li, X. Lu, X. Zhu, et al., Fiber laser butt joining of AZ31B alloy to 304 stainless steels with copper foil, Opt. Laser Technol. 117 (2019) 215–226, https://doi.org/10.1016/j.optlastec.2019.04.027.
[16] L. Liu, X. Qi, Z. Zhang, The effect of alloying elements on the shear strength of the lap joint of AZ31B magnesium alloy to Q235 steel by hybrid laser-TIG welding technique, Metall. Mater. Trans. A. 43 (2012) 1976–1988, https://doi.org/10.1007/s11661-011-1071-7.
[17] X. Zhao, C. Tan, L. Xiao, et al., Effect of the Ni coating thickness on laser welding-brazing of Mg/steel, J. Alloys Compd. 769 (2018) 1042–1058, https://doi.org/10.1016/j.jallcom.2018.08.080.
[18] A.M. Nasiri, P. Chartrand, D.C. Weckman, et al., Thermochemical analysis of phases formed at the interface of a Mg alloy-Ni-plated steel joint during laser brazing, Metall. Mater. Trans. A. 44 (2013) 1937–1946, https://doi.org/10.1007/s11661-012-1520-y.
[19] L. Liu, X. Qi, Z. Wu, Microstructural characteristics of lap joint between magnesium alloy and mild steel with and without the addition of Sn element, Mater. Lett. 64 (2010) 89–92, https://doi.org/10.1016/j.matlet.2009.10.023.
[20] H. Kasai, Y. Morisada, H. Fujii, Dissimilar FSW of immiscible materials: Steel/magnesium, Mater. Sci. Eng. A. 624 (2015) 250–255, https://doi.org/10.1016/j.msea.2014.11.060.
[21] Y. Wei, J. Li, J. Xiong, et al., Microstructures and mechanical properties of magnesium alloy and stainless steel weld-joint made by friction stir lap welding, Mater. Des. 33 (2012) 111–114, https://doi.org/10.1016/j.matdes.2011.07.016.
[22] Y. Meng, Y. Ma, S. Chen, et al., Friction stir butt welding of magnesium alloy to steel by truncated cone-shaped stirring pin with threads, J. Mater. Process. Technol. 291 (2021), https://doi.org/10.1016/j.jmatprotec.2020.117038.
[23] T. Wang, D. Ramírez-Tamayo, X. Jiang, et al., Effect of interfacial characteristics on magnesium to steel joint obtained using FAST, Mater. Des. 192 (2020) 108697, https://doi.org/10.1016/j.matdes.2020.108697.
[24] H. Das, P. Upadhyay, T. Wang, et al., Interfacial reaction during friction stir assisted scribe welding of immiscible Fe and Mg alloy system, Sci. Rep. 11 (2021) 1588, https://doi.org/10.1038/s41598-021-81266-9.
[25] B. Lang, D. Sun, G. Li, et al., Effects of welding parameters on microstructure and mechanical properties of resistance spot welded magnesium alloy joints, Sci. Technol. Weld. Join. 13 (2008) 698–704, https://doi.org/10.1179/174329307X249324.
[26] K. Zhang, L. Wu, C. Tan, et al., Influence of Al-Si coating on resistance spot welding of Mg to 22MnB5 boron steel, J. Mater. Process. Technol. 271 (2019) 23–35, https://doi.org/10.1016/j.jmatprotec.2019.03.024.
[27] L. Liu, L. Xiao, J. Feng, et al., The mechanisms of resistance spot welding of magnesium to steel, Metall. Mater. Trans. A. 41 (2010) 2651–2661, https://doi.org/10.1007/s11661-010-0333-0.
[28] V.K. Patel, S.D. Bhole, D.L. Chen, Characterization of ultrasonic spot welded joints of Mg-to-galvanized and ungalvanized steel with a tin interlayer, J. Mater. Process. Technol. 214 (2014) 811–817, https://doi.org/10.1016/j.jmatprotec.2013.11.028.
[29] Z. Xu, D.R. Ni, Q. Yang, et al., Influencing mechanism of Al-containing Zn coating on interfacial microstructure and mechanical properties of friction stir spot welded Mg–steel joint, Mater. Charact. 140 (6) 197–206. 10.1016/j.matchar.2018.04.011.
[30] T. Liyanage, J. Kilbourne, A.P. Gerlich, et al., Joint formation in dissimilar Al alloy/steel and Mg alloy/steel friction stir spot welds, Sci. Technol. Weld. Join. 14 (2009) 500–508, https://doi.org/10.1179/136217109X456960.
[31] J. Shen, S.B.M. Lage, U.F.H. Suhuddin, et al., Texture Development and Material Flow Behavior During Refill Friction Stir Spot Welding of AlMgSc, Metall. Mater. Trans. Phys. Metall. Mater. Sci. 49 (2018) 241–254, https://doi.org/10.1007/s11661-017-4381-6.
[32] X. Meng, Y. Huang, J. Cao, et al., Recent progress on control strategies for inherent issues in friction stir welding, Prog. Mater. Sci. 115 (2021), https://doi.org/10.1016/j.pmatsci.2020.100706.
[33] Z. Shen, Y. Ding, A.P. Gerlich, Advances in friction stir spot welding, Crit. Rev. Solid State Mater. Sci. 45 (2020) 457–534, https://doi.org/10.1080/10408436.2019.1671799.
[34] C. Gao, Y. Ma, L.-Z. Tang, et al., Microstructural evolution and mechanical behavior of friction spot welded 2198–T8 Al-Li alloy during aging treatment, Mater. Des. 115 (2017) 224–230, https://doi.org/10.1016/j.matdes.2016.11.045.
[35] J.Y. Cao, M. Wang, L. Kong, et al., Microstructure, texture and mechanical properties during refill friction stir spot welding of 6061–T6 alloy, Mater. Charact. 128 (2017) 54–62, https://doi.org/10.1016/j.matchar.2017.03.023.
[36] L.C. Campanelli, U.F.H. Suhuddin, A.Í.S. Antonialli, et al., Metallurgy and mechanical performance of AZ31 magnesium alloy friction spot welds, J. Mater. Process. Technol. 213 (2013) 515–521, https://doi.org/10.1016/j.jmatprotec.2012.11.002.
[37] U.F.H. Suhuddin, V. Fischer, J.F. dos Santos, The thermal cycle during the dissimilar friction spot welding of aluminum and magnesium alloy, Scr. Mater. 68 (2013) 87–90, https://doi.org/10.1016/j.scriptamat.2012.09.008.
[38] Y. Wang, P.B. Prangnell, Evaluation of Zn-rich coatings for IMC reaction control in aluminum-magnesium dissimilar welds, Mater. Charact. 139 (2018) 100–110, https://doi.org/10.1016/j.matchar.2018.02.035.
[39] J. Shen, U.F.H. Suhuddin, M.E.B. Cardillo, et al., Eutectic structures in friction spot welding joint of aluminum alloy to copper, Appl. Phys. Lett. 104 (2014), https://doi.org/10.1063/1.4876238 191901.
[40] Z. Shen, Y. Ding, J. Chen, et al., Interfacial bonding mechanism in Al/coated steel dissimilar refill friction stir spot welds, J. Mater. Sci. Technol. 35 (2019) 1027–1038, https://doi.org/10.1016/j.jmst.2019.01.001.
[41] P. Li, S.u. Chen, H. Dong, et al., Interfacial microstructure and mechanical properties of dissimilar aluminum/steel joint fabricated via refilled friction stir spot welding, J. Manuf. Process. 49 (2020) 385–396, https://doi.org/10.1016/j.jmapro.2019.09.047.
[42] H. Dong, S. Chen, Y. Song, et al., Refilled friction stir spot welding of aluminum alloy to galvanized steel sheets, Mater. Des. 94 (2016) 457–466, https://doi.org/10.1016/j.matdes.2016.01.066.
[43] G.S. Vacchi, R. Silva, A.H. Plaine, et al., Refill friction stir spot welded AA5754-H22/Ti-6Al-4V joints: Microstructural characterization and electrochemical corrosion behavior of aluminum surfaces, Mater. Today Commun. 22 (2020), https://doi.org/10.1016/j.mtcomm.2019.100759.
[44] K.e. Chen, B. Chen, S. Zhang, et al., Friction spot welding between porous TC4 titanium alloy and ultra high molecular weight polyethylene, Mater. Des. 132 (2017) 178–187, https://doi.org/10.1016/j.matdes.2017.06.071.
[45] Z. Shen, Y. Ding, J. Chen, et al., Comparison of fatigue behavior in Mg/Mg similar and Mg/steel dissimilar refill friction stir spot welds, Int. J. Fatigue. 92 (2016) 78–86, https://doi.org/10.1016/j.ijfatigue.2016.06.033.
[46] Y. Chen, J. Chen, B. Shalchi Amirkhiz, et al., Microstructures and properties of Mg alloy/DP600 steel dissimilar refill friction stir spot welds, Sci. Technol. Weld. Join. 20 (2015) 494–501, https://doi.org/10.1179/1362171815Y.0000000033.
[47] A.R. Marder, The metallurgy of zinc-coated steel, Prog. Mater. Sci. 45 (2000) 191–271, https://doi.org/10.1016/S0079-6425(98)00006-1.
[48] S. Wang, X. Wei, J. Xu, et al., Strengthening and toughening mechanisms in refilled friction stir spot welding of AA2014 aluminum alloy reinforced by graphene nanosheets, Mater. Des. 186 (2020), https://doi.org/10.1016/j.matdes.2019.108212.
[49] A.P. Hammersley, FIT2D: a multi-purpose data reduction, analysis and visualization program, J. Appl. Crystallogr. 49 (2016) 646–652, https://doi.org/10.1107/S1600576716000455.
[50] L. Lutterotti, S. Matthies, H.-R. Wenk, et al., Combined texture and structure analysis of deformed limestone from time-of-flight neutron diffraction spectra, J. Appl. Phys. 81 (1997) 594–600, https://doi.org/10.1063/1.364220.
[51] American National Standard AWS D17.2/D17.2M:2013, Specification for resistance welding for aerospace applications, American Welding Society, 2013.
[52] M. Esmaily, J.E. Svensson, S. Fajardo, et al., Fundamentals and advances in magnesium alloy corrosion, Prog. Mater. Sci. 89 (2017) 92–193, https://doi.org/10.1016/j.pmatsci.2017.04.011.
[53] P. Ghosh, M. Mezbahul-Islam, M. Medraj, Critical assessment and thermodynamic modeling of Mg–Zn, Mg–Sn, Sn–Zn and Mg–Sn–Zn systems, Calphad. 36 (2012) 28–43, https://doi.org/10.1016/j.calphad.2011.10.007.
[54] H. Okamoto, Supplemental Literature Review of Binary Phase Diagrams: Cs-In, Cs-K, Cs-Rb, Eu-In, Ho-Mn, K-Rb, Li-Mg, Mg-Nd, Mg-Zn, Mn-Sm, O-Sb, and Si-Sr, J. Phase Equilibria Diffus. 34 (2013) 251–263, https://doi.org/10.1007/s11669-013-0233-2.
[55] X. Gao, J.F. Nie, Structure and thermal stability of primary intermetallic particles in an Mg–Zn casting alloy, Scr. Mater. 57 (2007) 655–658, https://doi.org/10.1016/j.scriptamat.2007.06.005.
[56] X. Wang, J. Ahn, C. Kaboglu, et al., Characterisation of composite-titanium alloy hybrid joints using digital image correlation, Compos. Struct. 140 (2016) 702–711, https://doi.org/10.1016/j.compstruct.2015.12.023.
[57] M. Costa, D. Verdera, C. Leitão, et al., Dissimilar friction stir lap welding of AA 5754–H22/AA 6082–T6 aluminium alloys: Influence of material properties and tool geometry on weld strength, Mater. Des. 87 (2015) 721–731, https://doi.org/10.1016/j.matdes.2015.08.066.

[58] A.H. Plaine, U.F.H. Suhuddin, N.G. Alcântara, et al., Microstructure and mechanical behavior of friction spot welded AA6181-T4/Ti6Al4V dissimilar joints, Int. J. Adv. Manuf. Technol. 92 (2017) 3703–3714, https://doi.org/10.1007/s00170-017-0439-2.
[59] N.K. Babu, S. Brauser, M. Rethmeier, et al., Characterization of microstructure and deformation behaviour of resistance spot welded AZ31 magnesium alloy, Mater. Sci. Eng. A. 549 (2012) 149–156, https://doi.org/10.1016/j.msea.2012.04.021.
[60] U.F.H. Suhuddin, V. Fischer, A. Kostka, et al., Microstructure evolution in refill friction stir spot weld of a dissimilar Al–Mg alloy to Zn-coated steel, Sci. Technol. Weld. Join. 22 (2017) 658–665.
[61] B. Fu, G. Qin, F. Li, et al., Friction stir welding process of dissimilar metals of 6061–T6 aluminum alloy to AZ31B magnesium alloy, J. Mater. Process. Technol. 218 (2015) 38–47, https://doi.org/10.1016/j.jmatprotec.2014.11.039.
[62] H. Su, C.S. Wu, A. Pittner, et al., Thermal energy generation and distribution in friction stir welding of aluminum alloys, Energy. 77 (2014) 720–731, https://doi.org/10.1016/j.energy.2014.09.045.
[63] A. Berche, C. Drescher, J. Rogez, et al., Thermodynamic measurements in the Mg–Zn system, J. Alloys Compd. 503 (2010) 44–49, https://doi.org/10.1016/j.jallcom.2010.05.001.
[64] Z. Shen, W.Y. Li, Y. Ding, et al., Material flow during refill friction stir spot welded dissimilar Al alloys using a grooved tool, J. Manuf. Process. 49 (2020) 260–270, https://doi.org/10.1016/j.jmapro.2019.11.029.
[65] H.F. Zhang, L. Zhou, G.H. Li, et al., Prediction and validation of temperature distribution and material flow during refill friction stir spot welding of AZ91D magnesium alloy, Sci. Technol. Weld. Join. 26 (2021) 153–160, https://doi.org/10.1080/13621718.2020.1864864.
[66] G.-H. Li, L. Zhou, L. Luo, et al., Material flow behavior and microstructural evolution during refill friction stir spot welding of alclad 2A12-T4 aluminum alloy, Int. J. Miner. Metall. Mater. 28 (2021) 131–141, https://doi.org/10.1007/s12613-020-1998-z.
[67] N. Takata, M. Nishimoto, S. Kobayashi, et al., Crystallography of Fe2Al5 phase at the interface between solid Fe and liquid Al, Intermetallics. 67 (2015) 1–11, https://doi.org/10.1016/j.intermet.2015.07.011.
[68] M.-X. Zhang, P.M. Kelly, M. Qian, et al., Crystallography of grain refinement in Mg–Al based alloys, Acta Mater. 53 (2005) 3261–3270, https://doi.org/10.1016/j.actamat.2005.03.030.
[69] L. Liu, L. Xiao, J. Feng, et al., Bonding of immiscible Mg and Fe via a nanoscale Fe2Al5 transition layer, Scr. Mater. 65 (2011) 982–985, https://doi.org/10.1016/j.scriptamat.2011.08.026.
[70] Fu Banglong, Shen Junjun, Suhuddin Uceu F.H.R., Chen Ting, dos Santos Jorge F., Klusemann Benjamin, Rethmeier Michael, Improved mechanical properties of cast Mg alloy welds via texture weakening by differential rotation refill friction stir spot welding, Scripta Materialia 203 (2021) 114113, https://doi.org/10.1016/j.scriptamat.2021.114113.